RESEARCH ARTICLE

Dynamic Glycoprotein Hyposialylation Promotes Chemotherapy Evasion and Metastatic Seeding of Quiescent Circulating Tumor Cell Clusters in Breast Cancer

Nurmaa K. Dashzeveg[1], Yuzhi Jia[1], Youbin Zhang[2], Lorenzo Gerratana[3], Priyam Patel[4], Asif Shajahan[5], Tsogbadrakh Dandar[1], Erika K. Ramos[1], Hannah F. Almubarak[1], Valery Adorno-Cruz[1], Rokana Taftaf[1], Emma J. Schuster[1], David Scholten[1], Michael T. Sokolowski[1], Carolina Reduzzi[2,6], Lamiaa El-Shennawy[1], Andrew D. Hoffmann[1], Maroua Manai[2], Qiang Zhang[2], Paolo D'Amico[2], Parastoo Azadi[5], Karen J. Colley[7], Leonidas C. Platanias[2,8], Ami N. Shah[2,8], William J. Gradishar[2,8], Massimo Cristofanilli[2,6,8], William A. Muller[8,9], Brian A. Cobb[10], and Huiping Liu[1,2,8]

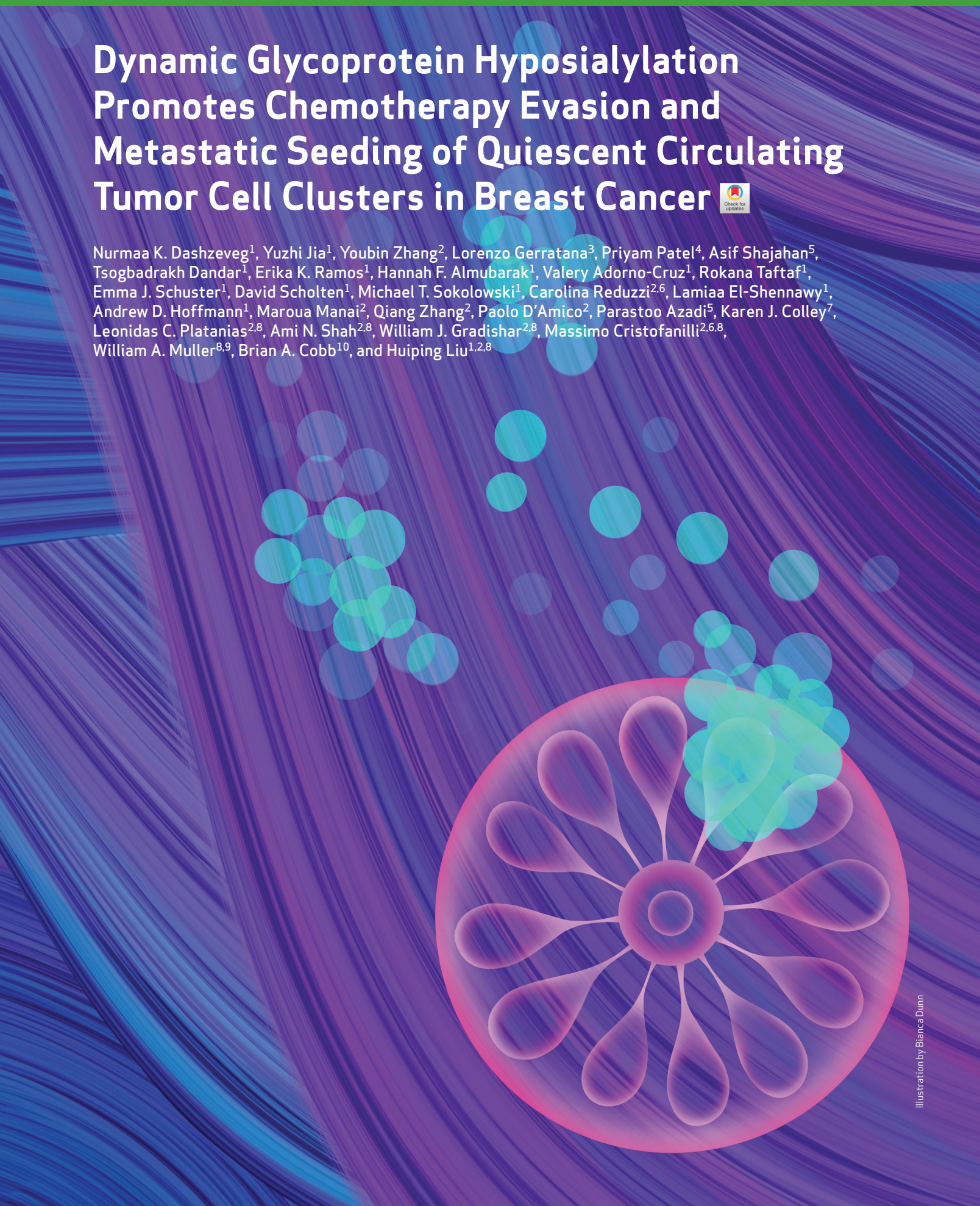

Illustration by Bianca Dunn

ABSTRACT Most circulating tumor cells (CTC) are detected as single cells, whereas a small proportion of CTCs in multicellular clusters with stemness properties possess 20- to 100-times higher metastatic propensity than the single cells. Here we report that CTC dynamics in both singles and clusters in response to therapies predict overall survival for breast cancer. Chemotherapy-evasive CTC clusters are relatively quiescent with a specific loss of ST6GAL1-catalyzed α2,6-sialylation in glycoproteins. Dynamic hyposialylation in CTCs or deficiency of ST6GAL1 promotes cluster formation for metastatic seeding and enables cellular quiescence to evade paclitaxel treatment in breast cancer. Glycoproteomic analysis reveals newly identified protein substrates of ST6GAL1, such as adhesion or stemness markers PODXL, ICAM1, ECE1, ALCAM1, CD97, and CD44, contributing to CTC clustering (aggregation) and metastatic seeding. As a proof of concept, neutralizing antibodies against one newly identified contributor, PODXL, inhibit CTC cluster formation and lung metastasis associated with paclitaxel treatment for triple-negative breast cancer.

SIGNIFICANCE: This study discovers that dynamic loss of terminal sialylation in glycoproteins of CTC clusters contributes to the fate of cellular dormancy, advantageous evasion to chemotherapy, and enhanced metastatic seeding. It identifies PODXL as a glycoprotein substrate of ST6GAL1 and a candidate target to counter chemoevasion-associated metastasis of quiescent tumor cells.

INTRODUCTION

Distant metastasis is often coupled with therapy evasion and a poor outcome for patients with cancer. Identifying the cellular mechanisms and molecular targets responsible for metastasis remains one of the most challenging frontiers in cancer medicine. Metastasis is seeded at an extremely low efficiency by single circulating tumor cells (CTC) but at a 20- to 100-fold higher efficiency by multicellular CTC clusters with stemness advantages, due in part to the plastic reprogramming, regenerative properties, and advantageous survival of clusters compared with single CTCs (1–5).

[1]Department of Pharmacology, Northwestern University Feinberg School of Medicine, Chicago, Illinois. [2]Department of Medicine, Division of Hematology and Oncology, Northwestern University Feinberg School of Medicine, Chicago, Illinois. [3]Department of Medicinal Oncology, Centro di Riferimento Oncologico di Aviano (CRO), IRCCS, Aviano, Italy. [4]Quantitative Data Science Core, Center for Genetic Medicine, Northwestern University Feinberg School of Medicine, Chicago, Illinois. [5]Complex Carbohydrate Research Center, University of Georgia, Athens, Georgia. [6]Division of Hematology-Oncology, Department of Medicine, Weill Cornell Medicine, New York, New York. [7]Department of Biochemistry and Molecular Genetics, University of Illinois Chicago, Chicago, Illinois. [8]Lurie Comprehensive Cancer Center, Northwestern University Feinberg School of Medicine, Chicago, Illinois. [9]Department of Pathology, Case Western Reserve University School of Medicine, Cleveland, Ohio. [10]Department of Pathology, Northwestern University Feinberg School of Medicine, Chicago, Illinois.

Corresponding Author: Huiping Liu, Departments of Medicine and Pharmacology, Division of Hematology and Oncology, Northwestern University Feinberg School of Medicine, Chicago, IL 60611. Phone: 312-503-5248; E-mail: huiping.liu@northwestern.edu

Cancer Discov 2023;13:2050–71

doi: 10.1158/2159-8290.CD-22-0644

Triple-negative breast cancer (TNBC) has a median overall survival of approximately 18 months (6) and is highly metastatic to viscera, such as the lungs (40%; ref. 7), which has been recapitulated in our established patient-derived xenograft (PDX) models (8). Although chemotherapy has been one of the first-line treatments for TNBC to shrink the primary tumor (9), the benefit of adjuvant chemotherapy might be limited and context-dependent (10–12). In phase III clinical trials for advanced or metastatic TNBC, about 55% of the patients might respond to chemotherapy such as paclitaxel (PAX) or nano-albumin–bound paclitaxel (PAX-NAB; ref. 13), with a median progression-free survival of 3 to 5 months (13, 14). In other large breast cancer trials, the addition of paclitaxel or taxol into a primary systemic or adjuvant therapy did not improve the distant disease-free survival or overall survival (OS) even after improving the response of the local disease to treatment (11, 12). In this study, we found that chemotherapy evasion (chemoevasion) is associated with enriched quiescent CTC clusters and possibly decreased survival for patients with breast cancer. As the microtubule inhibitor paclitaxel is used to treat metastatic breast cancer, we focused on determining its effects on CTCs.

Although collective migration and cohesive shedding could contribute to CTC cluster formation (1, 3), tumor cell aggregation (4, 15) provides an alternative mechanism to initiate and enhance tumor cluster formation (16). We previously demonstrated that cell adhesion and stemness glycoproteins on breast tumor-initiating cells, such as CD44, CD81, and ICAM1, drive CTC aggregation and homotypic cluster formation in metastatic TNBC (4, 15, 17). However, the role of glycosylation in CTC aggregation and cluster formation has yet to be fully elucidated.

Catalyzed by glycosyltransferases, glycosylation is one of the most common posttranslational protein modifications that add hierarchical sugar residues (monosaccharides or polysaccharide glycan chains) onto more than 50% of proteins (18, 19). To compare the glycan profiles between single and

clustered CTCs in patients, we utilized a spectrum of fluorophore-bound lectins with specific sugar residue–recognizing preferences for quantitative detection of sialic acids (SA), polylactosamine, galactose, complex type N-glycans, mannose, and fucose via flow cytometry and the FDA-approved CellSearch platform.

In this report, we found that terminal sugar residue α2,6-sialic acid (α2,6-SA) mediated glycoprotein sialylation, which is mainly catalyzed by β-galactoside α2,6-sialyltransferase (ST6GAL1) in human cells, specifically decreased in the CTC clusters surviving therapies. ST6GAL1 is a type II transmembrane protein that catalyzes the addition of α2,6-SA onto terminal glycans of glycoproteins (20). ST6GAL1 is known to regulate multiple hallmarks of cancer, such as promoting cell proliferation (21–24). This work identified a novel function of ST6GAL1, loss of which in CTCs promotes chemoevasion-associated cluster formation and metastatic seeding in TNBC. Furthermore, using advanced glycome mass spectrometry, we systemically analyzed α2,6-sialylated glycoproteins and identified many new substrates of ST6GAL1 related to cell adhesion or cancer stemness, such as PODXL, ICAM1, and CD44, which contribute to CTC aggregation and lung metastasis of TNBC. The evidence highlights new targeting strategies to block tumor cluster–mediated metastatic seeding associated with poor outcomes for TNBC.

RESULTS

Chemoevasive CTC Clusters Predict an Unfavorable Survival for Breast Cancer

To monitor the longitudinal dynamics of CTCs (singles and clusters) in response to therapy such as chemotherapy or paclitaxel, we established multiple complementary approaches in parallel, including (i) the standard CellSearch-based immunofluorescence staining of EpCAM-enriched $CD45^-$ cytokerain $(CK)^+DAPI^+$ cells from human blood; (ii) flow cytometry analysis of blood-derived $lineage^-CD45^-EpCAM^{+/-}CK^{+/-}$ cells, with singles and clusters gated on size scatter channels; and (iii) IHC staining of vascular CTCs in tissue sections (Supplementary Fig. S1A–S1C; refs. 4, 15).

After establishing an institutional review board–approved (IRB) protocol for longitudinal CTC analyses of patients with stage III–IV breast cancer at Northwestern University, we enrolled a cohort of 162 patients for blood collections at baseline prior to a new line of treatment (Supplementary Table S1A and S1B). Around half of the patients were followed up after 3 months of treatment for a second draw of blood and analysis of CTCs (singles and clusters) at the first radiologic evaluation [Evaluation 1 (E1)]. Blood was collected and analyzed for CTC counts (singles and clusters) on CellSearch (Supplementary Fig. S1B; Supplementary Excel S1). Consistent with the literature (3, 25) and our previous findings (4, 15), the detection of CTC clusters at baseline is associated with an unfavorable OS ($n = 162$, $P = 0.0003$; Supplementary Fig. S1D; Supplementary Table S1A). Among those with follow-up CTC monitoring and survival analysis ($n = 65$), the patients with decreased CTCs (single or clusters) at E1 showed the best OS compared with a moderate survival for those with stably low or negative counts of single CTCs/CTC clusters, and those with increased (or stably high counts) single CTCs/clusters at E1 after therapy showed the worst survival (Fig. 1A; Supplementary Fig. S1E). Using a multivariable Cox regression model, we found that CTC clusters at E1 is an independent factor predicting an unfavorable OS for patients with breast cancer (Supplementary Table S1B).

About half of the patients analyzed at E1 had received chemotherapy and the rest nonchemotherapy options (Supplementary Table S2). We compared the dynamic patterns of CTCs (singles and clusters) between baseline and E1 among chemotherapy and nonchemotherapy groups. The number of CTC clusters, but not single CTCs, increased significantly at E1 in the patients after chemotherapy ($n = 47$, Wilcoxon signed rank test $P = 0.0158$), whereas mixed fluctuations (without statistical significance) in CTCs (singles or clusters) were observed in the patients who did not receive new chemotherapy ($n = 35$; Fig. 1B; Supplementary Table S2). About 20% of the chemo-treated patients (8 out of 40) and ~10% of nonchemo-treated patients (3 out of 31) showed increased CTC clusters (or stable high) and worse survival in comparison with those with stably low (negative changes)

Figure 1. Chemotherapy correlates with CTC cluster formation and loss of α2,6-SA/ST6GAL1. **A,** The probability of OS by Kaplan–Meier estimates in the patients with advanced-stage breast cancer, stratified by three alteration patterns of single CTCs (left) or CTC clusters (middle) between baseline (prior to treatment) and the first radiologic evaluation (E1) after 3-month treatment, including (i) decreased CTCs; (ii) stably low or negative CTCs; and (iii) increased or stably high CTCs (singles or clusters). Wilcoxon signed-rank test $P < 0.0001$. CTCs were detected via CellSearch. Right, representative CellSearch images of a single CTC ($CK^+DAPI^+CD45^-$) at baseline (top row) and a two-cell CTC cluster at E1 (bottom) from a chemo-treated patient (scale bars = 10 μm). Dec, decreased; Inc, increased; Neg, negative. **B,** Dynamic counts of CellSearch-detected CTCs (# events), singles and CTC clusters, at baseline and E1 for each breast cancer patient treated with chemotherapy (blue lines) and nonchemotherapy options (purple lines). Wilcoxon signed rank test for CTC cluster alterations $P = 0.0158$ with chemo ($n = 47$) and $P = 0.6447$ without chemo ($n = 35$); for single CTC alterations $P = 0.5461$ with chemo and $P = 0.5028$ without chemo. **C,** The probability of OS by Kaplan–Meier estimates in patients with advanced-stage breast cancer with or without chemotherapy (chemo ±, left and right), stratified by the CTC alteration patterns of decreased, negative or stable low, and increased CTC cluster events at E1 compared with baseline (log-rank test $P = 0.0071$ and $P < 0.0001$). CTCs were measured by CellSearch. **D,** Representative images (left) and quantification (right) of Sambucus Nigra (SNA)–bound α2,6-SA signals in individual CTCs, both singles (S; $n = 120$ cells) and from clusters [C; $n = 44$ tumor cells in the clusters (homotypic and heterotypic clusters of CTCs and $CD45^+$ cells)] of patients with breast cancer ($n = 6$ patients), analyzed by CellSearch (scale bars = 10 μm). **E,** The bar graphs of SNA-high populations within singles (S) and clusters (C) in nonchemo-treated patients (left: –Chemo), chemo-treated patients (middle: +Chemo, $n = 46$, $P = 0.002$), and paclitaxel-treated patients (right: +PAX, $n = 6$, $P = 0.038$). **F,** Schematic of the PAX treatment for PDX-M1 tumors and subsequent analyses of CTCs and lung metastases (mets). One week after orthotopic implantation of PDX-M1 tumor cells into mouse mammary fat pads, mice were treated with PBS or PAX-NAB (PAX; 13.5 mg/kg) once every 3 days via tail vein 10 times. Three days after the last treatment, mice were sacrificed with collections of blood, breast tumors, and lungs for analyses of CTCs, tumors, and metastasis burdens, respectively. **G–N,** After PBS/PAX treatments shown in **F**, representative photos of PDX tumors (**G**; scale bars = 1 cm) and quantification of the tumor weight (**H**), bioluminescence images of dissected lungs *ex vivo* (**I**) and quantified lung metastases in total flux (**J**), counts of single CTCs (**K**) and CTC clusters (**L**) in PBS- and PAX-treated mice, and the percentage of SNA-high CTCs in singles vs. clusters in mice treated with PBS (**M**) and PAX (**N**). CTCs were analyzed via flow cytometry. *P* values were calculated by GraphPad (Student *t* test) unless otherwise indicated. Data, mean ± SD.

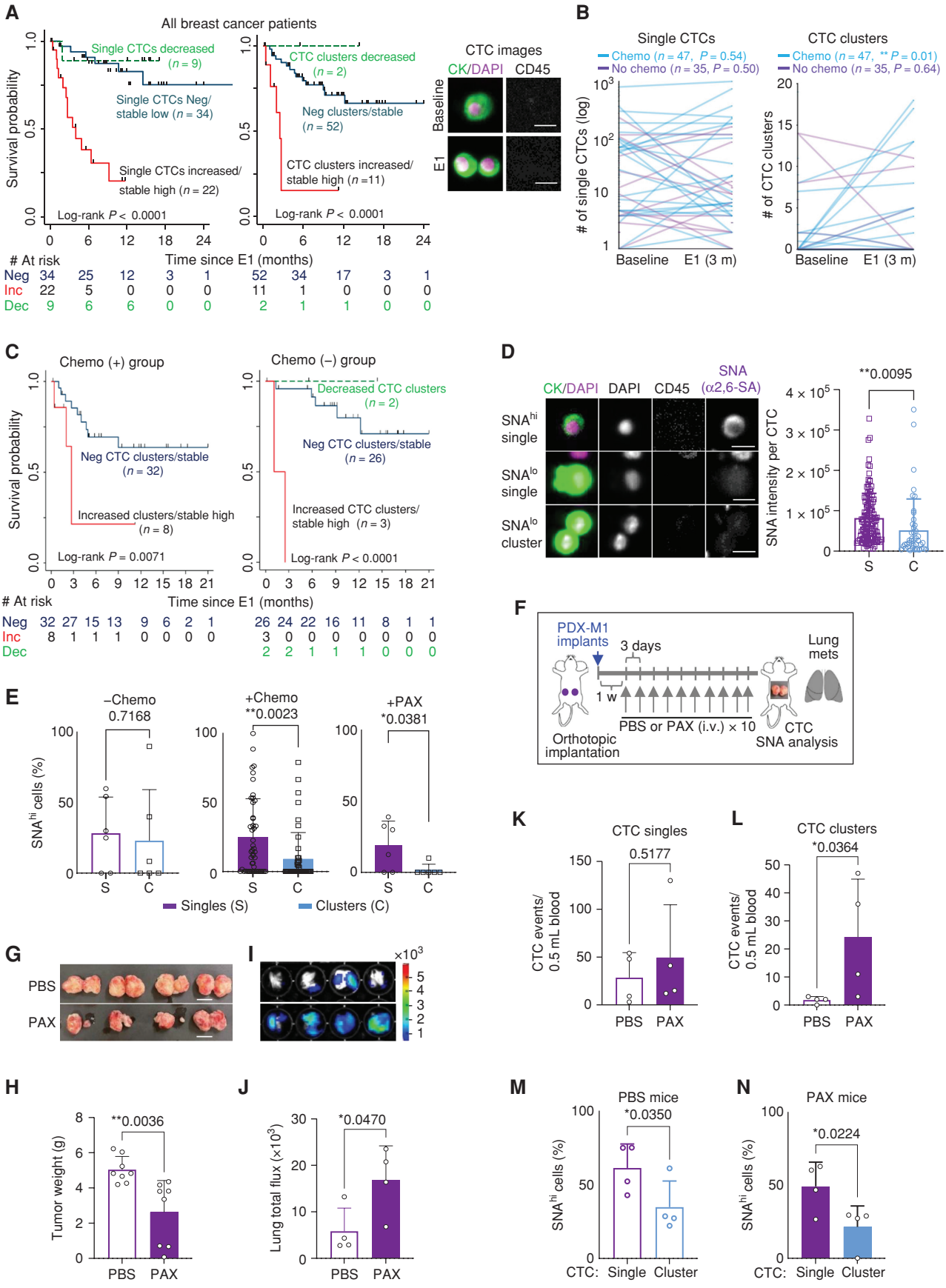
A
All breast cancer patients
Survival probability
Single CTCs decreased (n = 9)
Single CTCs Neg/ stable low (n = 34)
Single CTCs increased/ stable high (n = 22)
Log-rank P < 0.0001
CTC clusters decreased (n = 2)
Neg clusters/stable (n = 52)
CTC clusters increased/ stable high (n =11)
Log-rank P < 0.0001
CTC images
CK/DAPI CD45
Baseline
E1
At risk
Time since E1 (months)
Neg 34 25 12 3 1 52 34 17 3 1
Inc 22 5 0 0 0 11 1 0 0 0
Dec 9 6 6 0 0 2 1 1 0 0
B
Single CTCs
Chemo (n = 47, P = 0.54)
No chemo (n = 35, P = 0.50)
# of single CTCs (log)
Baseline E1 (3 m)
CTC clusters
Chemo (n = 47, ** P = 0.01)
No chemo (n = 35, P = 0.64)
# of CTC clusters
Baseline E1 (3 m)
C
Chemo (+) group
Survival probability
Neg CTC clusters/stable (n = 32)
Increased clusters/stable high (n = 8)
Log-rank P = 0.0071
Chemo (–) group
Decreased CTC clusters (n = 2)
Neg CTC clusters/stable (n = 26)
Increased CTC clusters/ stable high (n = 3)
Log-rank P < 0.0001
At risk
Time since E1 (months)
Neg 32 27 15 13 9 6 2 1 26 24 22 16 11 8 1 1
Inc 8 1 1 1 0 0 0 0 3 0 0 0 0 0 0 0
Dec 2 2 1 1 1 0 0 0
D
CK/DAPI DAPI CD45 SNA (α2,6-SA)
SNAhi single
SNAlo single
SNAlo cluster
SNA intensity per CTC
**0.0095
S C
E
–Chemo 0.7168
+Chemo **0.0023
+PAX *0.0381
SNAhi cells (%)
S C
Singles (S) Clusters (C)
F
PDX-M1 implants
3 days
1 w
PBS or PAX (i.v.) × 10
Orthotopic implantation
Lung mets
CTC SNA analysis
G
PBS
PAX
I
×10^3
H
Tumor weight (g)
**0.0036
PBS PAX
J
Lung total flux (×10^3)
*0.0470
PBS PAX
K
CTC singles
0.5177
CTC events/ 0.5 mL blood
PBS PAX
L
CTC clusters
*0.0364
CTC events/ 0.5 mL blood
PBS PAX
M
PBS mice
*0.0350
SNAhi cells (%)
CTC: Single Cluster
N
PAX mice
*0.0224
SNAhi cells (%)
CTC: Single Cluster

or decreased CTC clusters (Fig. 1C). Decreased CTC clusters were found only in the patients treated with nonchemo approaches (Fig. 1C, right) but not observed in the chemo-treated group (Fig. 1C, left). These data suggest that CTC clusters may confer therapy-resistant or chemoevasive features that have yet to be fully elucidated.

Loss of α2,6-Sialylation in Clustered CTCs and Associated with PAX Treatment

To investigate whether cell-surface glycosylation impacts CTC cluster formation, we first optimized the flow cytometry approach to analyze the glycosylation profiles in $EpCAM^{+/-}$ $CK^{+/-}CD45^{-}$ CTCs (clusters and singles) using lectin-based recognition of various carbohydrate residues. These include the terminal sialylation residues α2,3-SA and α2,6-SA [recognized by lectins MAL-II and Sambucus Nigra (SNA), respectively], polylacto-samine (LEL), galactose (RCA), tri- and tetra-antennary complex type N-glycans (PHA-L), mannose (ConA), and fucose (LTL; Supplementary Fig. S2A). Among all tested glycans, the levels of SNA-bound α2,6-SA had the most dramatic reduction in clustered CTCs along with a moderate decrease of α2,3-SA and fucose levels compared with single CTCs from patients with breast cancer ($n = 60$, $P < 0.0001$), whereas the single and clustered white blood cells ($CD45^{+}$) had comparable levels for tested glycans (Supplementary Fig. S2B–S2E; Supplementary Excel S2). Consistently, when analyzed on the CellSearch platform, $CK^{+}DAPI^{+}CD45^{-}$CTCs in the clusters displayed lower α2,6-SA levels (SNA binding) per cell than the singles (Fig. 1D), confirming the flow analysis data. Moreover, in comparison with single CTCs, α2,6-SA levels specifically decreased in the CTC clusters of chemo-treated and paclitaxel (PAX)-treated patient groups, but not in the nonchemo-treated group (Fig. 1E), implicating an association of hyposialylation with chemotherapy or PAX treatment.

As a proof of concept, we treated mice with PAX following orthotopic implantation of luciferase 2-eGFP (L2G)– or luciferase 2-tdTomato (L2T)–labeled TNBC PDX cells (8) into the fourth mammary fat pads (Fig. 1F). The tumor sizes were slightly reduced in response to PAX treatment (Fig. 1G and H); however, the spontaneous metastases to the lungs were significantly higher in the PAX-treated group than in the control PBS–treated group (Fig. 1I and J). Blood analysis of $L2G^{+}$ or $L2T^{+}$ CTC via flow cytometry did not identify significant changes in the total number of single CTCs between the two groups of mice (Fig. 1K), whereas the events of CTC clusters were significantly higher in the PAX-treated group than in the PBS control group (Fig. 1L). CTC clusters displayed lower levels of α2,6-SA sialylation (SNA signals) than single CTCs in both groups (Fig. 1M and N). These findings suggest that chemoevasive CTC clusters are associated with PAX treatment, enhanced lung metastasis, and loss of α2,6-sialylation.

Loss of α2,6-SA or ST6GAL1 Promotes CTC Cluster Formation, Leading to the Evasion of PAX Treatment

To determine whether α2,6-SA levels and ST6GAL1 influence tumor cell clustering, we first sorted the SNA-high and SNA-low subpopulations from the metastatic MDA-MB-231 cells (Fig. 2A; Supplementary Videos S1 and S2). When seeded onto poly-HEMA–treated plates for cell suspension and cluster formation assessment, the SNA-low cells aggregated into bigger clusters than SNA-high cells (Fig. 2A, right). Moreover, neuraminidase (NA)-mediated cleavage of SA (α2,6-SA, α2,3-SA, and α2,8-SA) from the cell surface also drastically promoted tumor cluster formation (Supplementary Fig. S3A and S3B). Because CD44 was one of the main adhesion molecules and breast tumor initiation markers mediating CTC cluster formation (4), we compared the glycan profiles in CD44 wild-type (WT) and CD44 knockout (KO) cells. CD44KO cells with compromised clustering capabilities increased α-2,6-SA levels and ST6GAL1 expression without altering other tested glycan residues (Supplementary Fig. S3C–S3F). CD44 overexpression inhibited ST6GAL1 expression in CD44KO cells and siST6GAL1 knockdown partially rescued the tumor cell formation of CD44KO cells (Supplementary Fig. S3G and S3H).

We continued to determine the regulatory effects of ST6GAL1 gene modulation (depletion and overexpression) on human and mouse tumor cell clustering. Both human *ST6GAL1* KO (ST6KO) tumor cells (MDA-MB-231 and PDXs) and mouse *St6gal1* KO (St6KO) tumor cells (4T1) were generated via CRISPR–Cas9 and specific gRNAs (generated by Dr. Derek W. Abbott at Case Western Reserve University). Using glycoproteomic mass spectrometry, we observed a complete depletion of the peaks of α2,6-SA on glycoproteins, whereas α2,3-SA peaks remained in ST6KO MDA-MB-231 cells in comparison with the WT cells (Supplementary Fig. S4A and S4B), consistent with the loss of sialic acid peaks in the LC-MS/MS spectra of the tryptic digest for extracted ion HexNAc and SA monosaccharide profiles, as well as loss of SNA binding to these cells in flow cytometry profiling (Fig. 2B, left; Supplementary Fig. S4C), suggesting a dominant role of ST6GAL1 in α2,6-SA of breast tumor cells.

Consistently, both ST6KO in human tumor cells and St6KO in mouse 4T1 tumor cells promoted the cluster formation of tumor cells in suspension compared with their WT controls (Fig. 2B; Supplementary Fig. S5A). When *ST6GAL1* was overexpressed (OE) in the ST6KO cells, the α2,6-SA levels were rescued with inhibited cluster formation (Fig. 2B; Supplementary Videos S3–S5). Similarly, the ST6GAL1 depletion–enhanced cluster formation was repeatedly observed in multiple ST6KO clones of MDA-MB-231 cells, as well as the cells with siRNA-mediated knockdown of ST6GAL1 (Supplementary Fig. S5B–S5E). These results suggest that CTC aggregation-based cluster formation is negatively associated with and inhibited by cell-surface α2,6-SA levels, as well as ST6GAL1.

We then investigated the effects of chemotherapy such as PAX on the levels of surface α2,6-SA and cluster formation of patient CTC-092–derived xenograft tumor cells (PDX; ref. 26) and MDA-MB-231 cells. Clinically used PAX in nano-albumin–bound version (PAX-NAB) at 25 to 50 μg/mL induced minimal cell death in CTC-092 cells *ex vivo*, with a small subset of SNA-high cells showing a selective vulnerability (<5%) to the high-dose treatment at 250 μg/mL (Fig. 2C; Supplementary Fig. S5F). As a result, PAX treatment decreased α2,6-SA levels (SNA binding) in a dose-dependent manner (Fig. 2D) and promoted cluster formation of chemo-resistant CTC-092 cells at a low dose of 25 μg/mL (Fig. 2E; Supplementary Videos S6 and S7). Next, we treated sorted SNA-high and SNA-low cells for PAX treatment and assessed cell viability. Although 35% of the cells in SNA-high populations died in

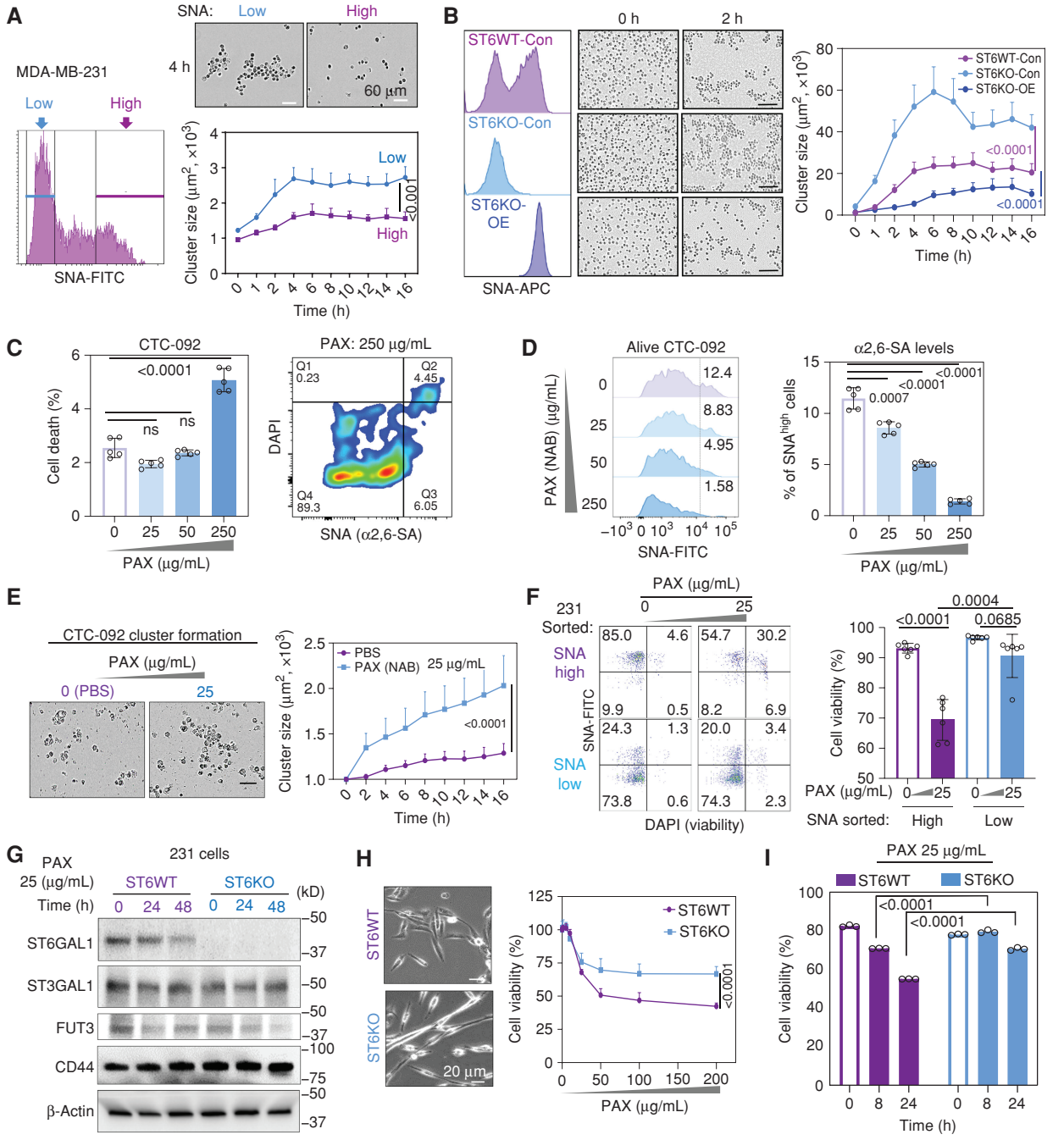

Figure 2. α2,6-SA and ST6GAL1 inhibit cluster formation and confer sensitivity to PAX. **A,** Left, flow profile of MDA-MB-231 cells with α2,6-SA–low and α2,6-SA–high populations. Right, representative images of sorted α-2,6-SA–low and α2,6-SA–high cells at 4 hours of clustering (top) and cluster formation curves (cluster size by area) of sorted cells (bottom). Scale bars = 60 μm. See Supplementary Videos S1 and S2 for cluster videos. **B,** Flow histograms of SNA-binding signals (left), representative cluster images (middle), and cluster formation curves (right) of MDA-MB-231 cells: ST6WT and ST6KO cells transfected with control vectors (-Con), and ST6KO cells transfected with ST6GAL1 overexpression vector (-OE). Scale bars = 100 μm. Cluster videos are available as Supplementary Videos S3–S5. **C,** Left: cell death (%) of CTC-092 PDX tumor cells *ex vivo* 24 hours after paclitaxel (PAX) treatments at 0, 25, 50, and 250 μg/mL, measured as DAPI positivity of live cells via flow cytometry (ns, not significant). Right, representative flow profile of DAPI and SNA signals in PAX-treated cells at the high dose of 250 μg/mL. **D,** Representative flow histograms (left) and SNA-high population (%) within alive CTC-092 cells (right) after 24 hours of PAX treatment at indicated doses (0–250 μg/mL). **E,** Representative images of CTC clusters formed at 24 hours (left) and the time-course cluster formation curves (right, cluster size) of CTC-092 PDX cells *ex vivo* upon treatment with PBS and PAX-NAB at 25 μg/mL. Scale bar = 50 μm. See Supplementary Videos S6 and S7 for cluster videos. **F,** Representative flow plots (left) and quantified viability (DAPI exclusion %; right graph) of flow sorting–enriched SNA-high and SNA-low MDA-MB-231 cells (as shown in **A**) after overnight treatment with PAX at 0 and 25 μg/mL. **G,** Immunoblots of ST6GAL1, ST3GAL1, FUT3, CD44, and β-actin (loading control) of ST6WT and ST6KO cells at indicated time points (0, 24, and 48 hours) after PAX (25 μg/mL) treatment. Data are representative images of 2 biological replicates. **H,** Bright-field images of ST6WT and ST6KO cells (left) and their cell viability (%) after treatment with PAX at indicated doses (0–200 μg/mL; right). **I,** Cell viability of ST6WT and ST6KO cells after indicated time of paclitaxel (PAX) treatment at 25 μg/mL. *P* values were calculated with the Student *t* test in GraphPad unless otherwise indicated. Data, mean ± SD of 3–5 experimental replicates.

response to PAX treatment, minimal cell death was observed in SNA-low populations (Fig. 2F), suggesting that α2,6-SA deficiency is associated with resistance and/or evasion to PAX treatment. Notably, PAX treatment selectively decreased ST6GAL1 protein expression over time without altering ST3GAL1 levels (Fig. 2G), although transient knockdown of ST3GAL1 (which catalyzes the transfer of α2,3-SA) via siRNAs had similar cluster-promoting effects as siST6GAL1 (Supplementary Fig. S5E), suggesting a distinct regulatory mechanism and chemo-selective pressure on ST6GAL1.

We further determined the effects of ST6GAL1 depletion on cancer cell sensitivity to therapeutic agents, including the chemotherapeutics PAX and doxorubicin as well as the CDK inhibitor palbociclib. Compared with ST6WT cells, ST6KO in MDA-MB-231 tumor cells enabled a specific resistance to PAX treatments (25–200 μg/mL; Fig. 2G–I), but with a similar sensitivity to palbociclib and a moderately increased sensitivity to doxorubicin (Supplementary Fig. S6A–S6D). When SNA-high (WT) and low (ST6KO) cells were mixed at a 1:1 ratio prior to treatment, increased dominance of the α2,6-SA–low (ST6KO) population of MDA-MB-231 cells emerged 24 hours after PAX treatment (25 μg/mL; Supplementary Fig. S6E), similar to the profiles of CTC-092 cells in response to PAX treatment (Fig. 2D).

Loss of ST6GAL1 Induces Quiescence in CTC Clusters for Chemoevasion

Next, we investigated if chemoevasion of the CTC clusters is associated with distinct proliferative status, as previous studies demonstrated that ST6GAL1 and α2,6-SA are associated with cellular proliferation in various cancers (27–29). We first added customized Ki-67 staining to the patient CTC panel analyses via CellSearch. Through binary assessment and intensity comparison, decreased Ki-67 positivity was observed in clustered CTCs in comparison with single CTCs from patients with breast cancer (Fig. 3A and B, $P = 0.0005$ and 0.008). The heterogeneous levels of Ki-67 signal intensity per cell in singles and clusters positively correlated with the DAPI signal intensity (DNA content) in each CTC (Fig. 3C). The cell-cycle analyses based on DAPI intensity revealed that the population of G_1–G_0 phase increased in clusters after chemotherapy (73%) more than that of single CTCs (59%), whereas single and clusters at baseline prior to therapy were 64% and 67%, respectively (Fig. 3D). Moreover, the intensity of DNA content (DAPI intensity) is in positive correlation with SNA signals (α2,6-SA levels) per human CTC (Fig. 3E). We then continued to measure the α2,6-SA levels and Ki-67 positivity of CTCs in TNBC PDX models that develop spontaneous lung metastases (4). Flow cytometry analyses revealed that the SNA-high levels (%) of $L2T^+/L2G^+$ CTCs from the PDX-M1 tumor-bearing mice also correlated with high Ki-67 positivity (Fig. 3F). Furthermore, in PAX-treated mice, the Ki-67 positivity (%) within CTC clusters was significantly lower than single CTCs (Fig. 3G), indicating an association of CTC clusters with low α2,6-SA levels and relative quiescence under the pressure of PAX treatment.

To further elucidate the transcriptome programs related to low α2,6-SA levels (ST6GAL1 depletion) and quiescence, we conducted RNA-sequencing (RNA-seq) analysis of the WT and ST6KO bulk tumor cells. Hallmark pathway analysis and gene set enrichment analysis identified differential regulatory pathways in ST6KO tumor cells, including suppressed cell cycling, such as E2F targets, G_2–M checkpoints, and MYC targets, as well as upregulated interferon responses, cell adhesion, epithelial-to-mesenchymal transition, and inflammatory responses (Fig. 3H–J; Supplementary Fig. S7A–S7C; Supplementary Excel S3). As the RB–E2F signaling pathway controls proliferation and quiescence in cancer cells (30–32), we analyzed cell growth and cell-cycle phases of the tumor cells using multiple approaches. ST6KO cells showed a delayed growth rate for confluency compared with the WT cells (Fig. 3K). Using Hoechst and pyronin Y–based DNA and RNA (respectively) double staining, we found that α2,6-SA–low (SNA-low) WT cells dominated the quiescent pyronin Y^- (G0) phase but contributed to only a small subset of active cycling phases, G_1, S, and G_2–M (Fig. 3L). Furthermore, compared with ST6WT cells, ST6KO increased the proportion of tumor cells in quiescent/G_0 phase and decreased in active cell cycles such as G_1 and G_2–M (Fig. 3M and N), with a consistent pattern of delayed and halted cell division with relatively undiluted dye of carboxyfluorescein succinimidyl ester (CFSE) in the KO cells (Supplementary Fig. S8A). Furthermore, ST6KO cells formed significantly smaller colonies than ST6WT cells (Supplementary Fig. S8B). When ST6WT and KO cells were mixed in two distinct colors for competitive proliferation assays in culture (Supplementary Fig. S8C), the counts of ST6KO cells were overtaken by ST6WT cells over time (Supplementary Fig. S8D–S8G). However, the dominance was converted to ST6KO cells under PAX treatment at an even lower dose of 25 μg/mL (Supplementary Fig. S6E). These results suggest that lack of ST6GAL1 induces cellular quiescence at G_0 and provides advantages to chemoevasion.

Because chemoresistance is often associated with local relapse and distant metastasis, we continued to investigate the clinical relevance of α2,6-SA and ST6GAL1 levels in CTCs or tumor cells with breast cancer outcomes. Clinically, we observed an unfavorable distant metastasis–free survival (since the diagnosis) of the patients with breast cancer and detectable SNA-low CTCs (Supplementary Fig. S8H). Furthermore, using the online Kaplan–Meier plotter analysis (33), we found that high expression of *ST6GAL1* mRNAs is associated with a favorable relapse-free survival in TNBC ($n = 265$, $P = 0.019$) and higher protein levels of ST6GAL1 in breast cancer predict a dramatically better OS than those with lower protein levels ($n = 65$, $P = 0.0096$; Supplementary Fig. S8I and S8J). These data prompted us to investigate the alteration patterns and molecular mechanisms associated with the impact of ST6GAL1 in metastasis.

Dynamic Changes of α2,6-SA and ST6GAL1 Levels in CTCs and Disseminated Tumor Cells during Seeding

To determine the patterns of α2,6 sialylation in CTCs and disseminated tumor cells (DTC) during metastasis, we compared their ST6GAL1 expression profiles and α2,6-SA levels using IHC staining and flow cytometry, respectively. In PDX-M1 orthotopic tumor models, the lung tissue sections with spontaneous metastases were stained with anti-human ST6GAL1, showing a significantly higher ST6GAL1 positivity (%) in single CTCs and DTCs than CTC clusters

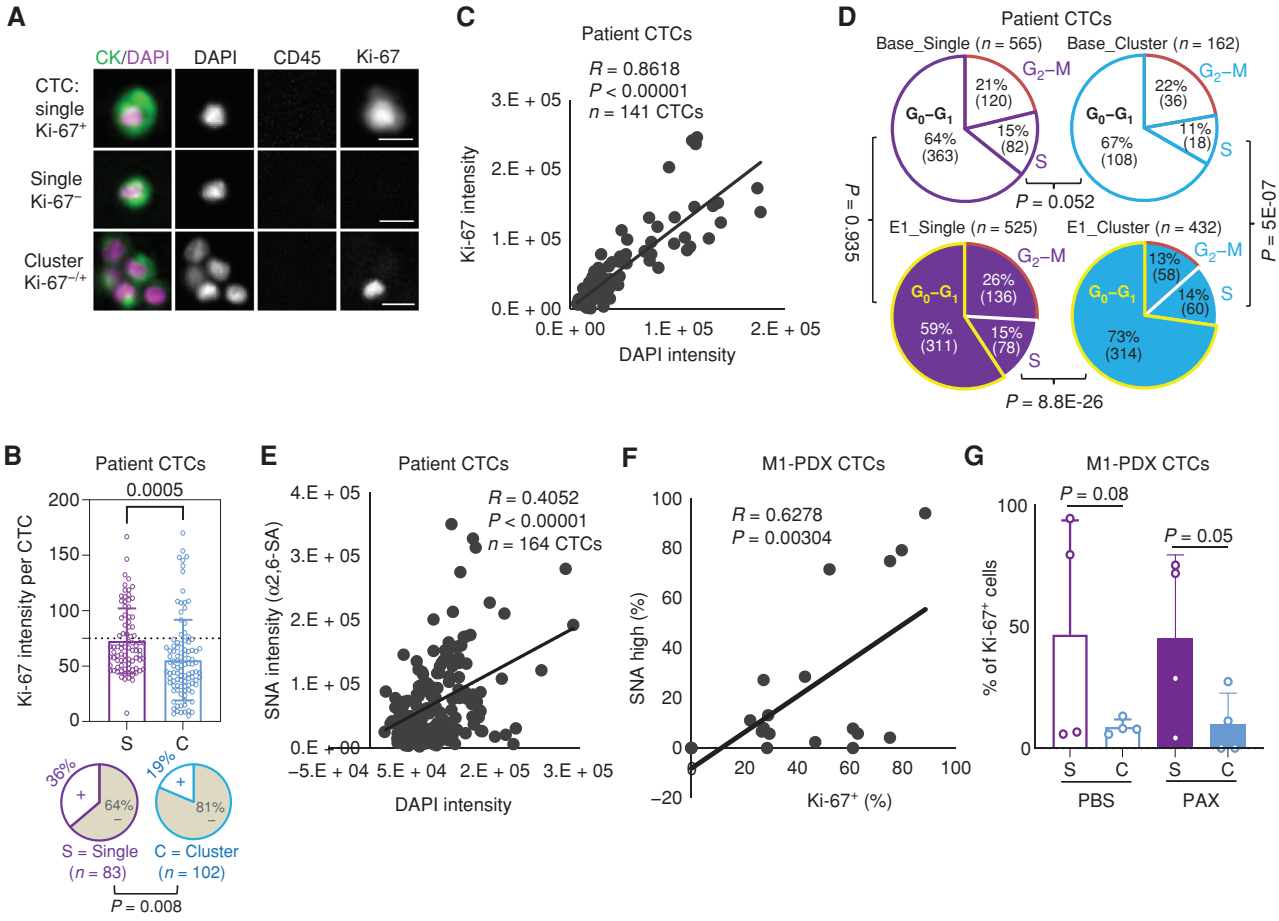

Figure 3. Lack of α2,6-SA and ST6GAL1 is associated with quiescence in CTC clusters. **A,** Representative CellSearch CTC ($CK^+DAPI^+CD45^-$) images of two singles and one 5-cell cluster with channels of CK/DAPI merged, DAPI, CD45, and Ki-67 signals, collected from the blood of patients with breast cancer. One single CTC and one CTC within the cluster stained Ki-67 positive. Scale bars = 10 μm. **B,** Ki-67 signal intensity per cell in single CTCs ($n = 83$ cells) and clustered CTCs ($n = 102$ cells, $P = 0.0005$), as well as binary assessment of Ki-67–positive cells (positive threshold at the intensity mean >75) between single CTCs and CTC clusters ($P = 0.008$), as measured on ImageJ. **C,** Plots of individual CTCs showing a positive association between quantified Ki-67 (proliferative index) and DAPI (DNA content) signal intensities per CTC ($n = 141$, $R = 0.8618$, $P < 0.00001$, calculated using www.socscistatistics.com), as measured on ImageJ. **D,** Proportion of single and clustered CTC distributions within the cell-cycle phases (G_0–G_1, S, G_2–M) at baseline and E1 after treatment, based on the DAPI (DNA) intensity of each CTC on ImageJ using CellSearch images. The ranges of DAPI mean intensity/cell: $G_1/G_0 < 100$, S = 100–140, G_2–M > 140 ($n = 1{,}684$ CTCs from 15 patients with breast cancer), $P = 0.052$ (baseline singles vs. baseline clusters), $P = 8.8E\text{-}26$ (E1 singles vs. E1 clusters), $P = 0.935$ (baseline singles vs. E1 singles), and $P = 5.2E\text{-}07$ (baseline clusters vs. E1 clusters). **E,** Dot plots of individual CTCs with a positive correlation between SNA signals (α2,6-SA) and DAPI intensity (DNA content) per CTC ($n = 164$ cells, $R = 0.4052$, $P < 0.00001$). **F** and **G,** Pearson correlation of the percentage (%) of SNA-high cells and % of $Ki\text{-}67^+$ CTCs in M1-PDX tumor-bearing mice ($n = 20$ mice, $R = 0.6278$, $P < 0.00304$ calculated using www.socscistatistics.com; **F**) and the % of $Ki\text{-}67^+$ CTCs in singles vs. clusters (**G**) in the PBS/PAX-treated PDX-M1 model shown in Fig. 1F–N. (*continued on next page*)

(Supplementary Fig. S9A and S9B). Analyses of SNA binding to $eGFP^+$ ($L2G^+$) or $tdTomato^+$ ($L2T^+$) primary tumor cells, CTCs, and lung metastases from TNBC PDX-M1 also revealed lower α2,6-SA levels in CTCs than both primary tumor cells and lung metastases, which regained higher levels of α2,6 sialylation after seeding (Supplementary Fig. S9C). Single-cell RNA-seq of primary tumor cells, CTCs, and lung metastasis from our PDXs and MDA-MB-231 tumors (4) also revealed low expression of ST6GAL1 in CTCs (Supplementary Fig. S9D), suggesting possible plasticity and dynamic α2,6 sialylation patterns in CTCs during metastatic seeding. Then, we sorted SNA-high and SNA-low cells of MDA-MB-231 cells for tail-vein injection into mice, and the lungs were dissected and dissociated for flow cytometry analyses of $L2G^+/L2T^+$ tumor cells. Surprisingly, the SNA-low tumor cells (sorted as 100% SNA-low) shifted to nearly all SNA-high (>90% high) DTCs in the lungs, as detected at 24 hours and 9 days after intravenous injection (Supplementary Fig. S9E and S9F), suggesting a transient loss of α2,6-SA in CTCs and a dynamic gaining of sialylation in DTCs after seeding. This finding led us to determine the regulatory roles of ST6GAL1 in metastasis in TNBC.

Depletion of ST6GAL1 Promotes Metastatic Seeding of TNBC

Based on the glycan profiles of multiple TNBC PDX tumors (8), we identified SNA-high M1 and M3 PDXs (>95% SNA^+) and SNA-low M2 PDXs (~45% SNA^+; Fig. 4A), which

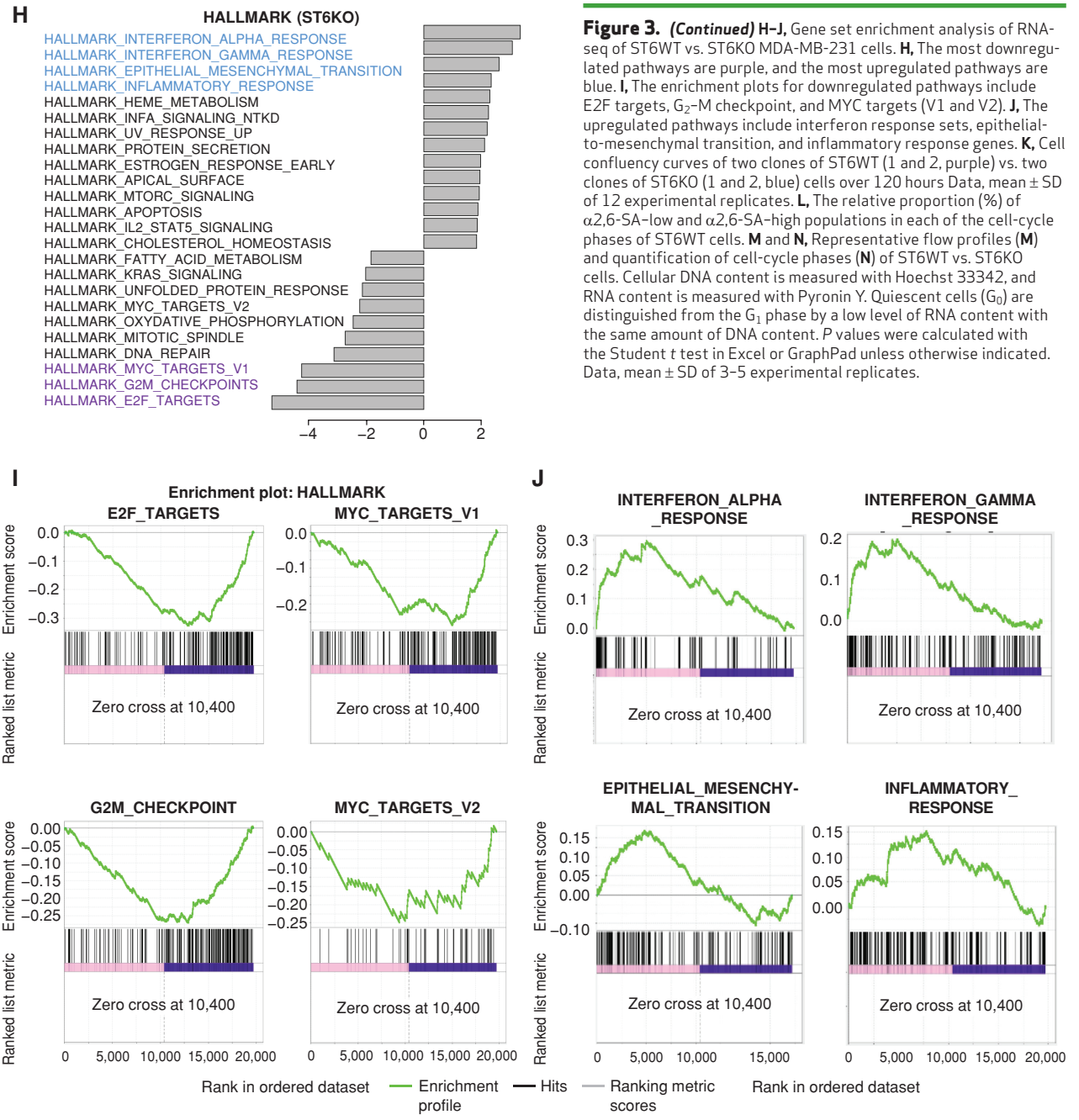

Figure 3. ***(Continued)*** **H–J,** Gene set enrichment analysis of RNA-seq of ST6WT vs. ST6KO MDA-MB-231 cells. **H,** The most downregulated pathways are purple, and the most upregulated pathways are blue. **I,** The enrichment plots for downregulated pathways include E2F targets, G_2–M checkpoint, and MYC targets (V1 and V2). **J,** The upregulated pathways include interferon response sets, epithelial-to-mesenchymal transition, and inflammatory response genes. **K,** Cell confluency curves of two clones of ST6WT (1 and 2, purple) vs. two clones of ST6KO (1 and 2, blue) cells over 120 hours Data, mean ± SD of 12 experimental replicates. **L,** The relative proportion (%) of α2,6-SA–low and α2,6-SA–high populations in each of the cell-cycle phases of ST6WT cells. **M** and **N,** Representative flow profiles (**M**) and quantification of cell-cycle phases (**N**) of ST6WT vs. ST6KO cells. Cellular DNA content is measured with Hoechst 33342, and RNA content is measured with Pyronin Y. Quiescent cells (G_0) are distinguished from the G_1 phase by a low level of RNA content with the same amount of DNA content. *P* values were calculated with the Student *t* test in Excel or GraphPad unless otherwise indicated. Data, mean ± SD of 3–5 experimental replicates.

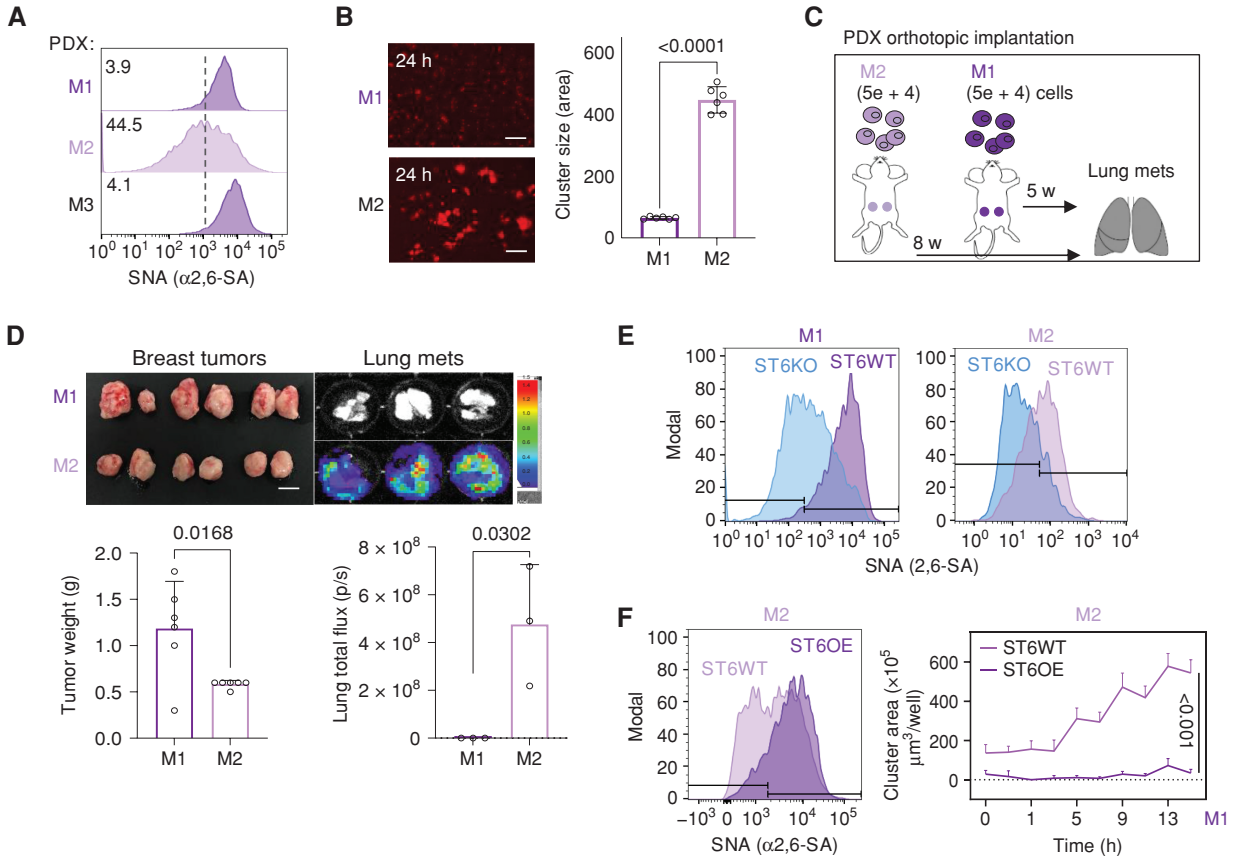

Figure 4. ST6GAL1 inhibits cluster formation and blocks metastatic seeding in PDX models. **A,** Flow cytometry profiles of α2,6-SA (SNA) of indicated PDX models (M1, M2, and M3). **B,** Representative images (left) and quantification (right) of cluster size (area) of PDX-M1 (M1) vs. PDX-M2 (M2) tumor cells at 24 hours (scale bars = 300 μm). Data are represented as mean ± SD of 6 experimental replicates. **C,** Schematic design to analyze spontaneous metastases of M1 (–5 weeks) and M2 (–8 weeks) PDX tumor models: 5×10^4 cells were orthotopically injected into the fourth mouse mammary fat pads. Five to 8 weeks after implantation, breast tumor weight and lung metastases (mets) were measured. **D,** Top: images of dissected tumors (scale bar = 1 cm) and lung metastases (bioluminescence) of M1 and M2 PDX models. Bottom: quantified tumor weight (g) and lung metastasis (bioluminescence imaging total flux). **E,** Flow cytometry profiles of α2,6-SA levels in ST6WT and ST6KO PDX-M1/M2 models. **F,** Flow cytometry profile of α2,6-SA levels (left) and cluster formation curves (right) in ST6WT and ST6OE cells derived from M2 PDXs. Curve data are represented as mean ± SD of 12 experimental replicates. (*continued on next page*)

were labeled by the dual optical reporters L2G or L2T (8) for bioluminescence and fluorescence imaging (4). When placed on collagen-coated plates *ex vivo* for aggregation-based clustering (4), dissociated SNA-low M2 tumor cells formed 5-fold larger clusters than the SNA-high M1 tumor cells (Fig. 4B). To compensate for the potential disadvantages of smaller tumors for metastasis, we designed a series of tumor implantation experiments for slow-growing ST6-deficient tumor cells to reach tumor volumes relatively close to ST6WT or SNA-high tumors for assessment of metastatic seeding and lung colonization. To determine the regulatory roles of ST6GAL1, the entire *in vivo* metastatic analysis of both ST6WT and ST6KO cells is shown in Supplementary Fig. S10A.

We first compared the lung metastases developed by SNA-high M1 and SNA-low M2 PDX models (Fig. 4C). Following orthotopic implantations of equal numbers of tumor cells into mouse mammary fat pads but at different timing, we observed a slower growth rate of the SNA-low M2 PDXs, which within an even extended time window grew about half the weight of the SNA-high M1 tumors; however, these smaller M2 tumors developed spontaneous lung metastases with bioluminescence signals in 10^8-fold higher intensity than that of M1 PDXs (Fig. 4D), suggesting that low α2,6-SA levels are associated with an elevated metastatic potential in PDX models. To determine if genetic modulations of ST6GAL1 and α2,6-SA levels impact lung metastasis, we first generated ST6KO with depleted α2,6-SA levels in M1 and M2 PDXs (Fig. 4E) but also overexpressed ST6GAL1 (ST6OE) in SNA-low M2 PDX cells in which elevated α2,6-SA levels inhibited tumor cell cluster formation (Fig. 4F).

After tail-vein injections of equal numbers of tumor cells, ST6KO M1 and ST6KO M2 cells seeded 2.5-fold and 5-fold experimental metastases to the lungs within 24 hours compared with their respective ST6WT tumor cell controls (Fig. 4G and H). The elevated seeding of ST6KO tumor cells sustained in colonizing the lungs more effectively than the WT control cells, as detected 5 weeks after injections (Fig. 4I).

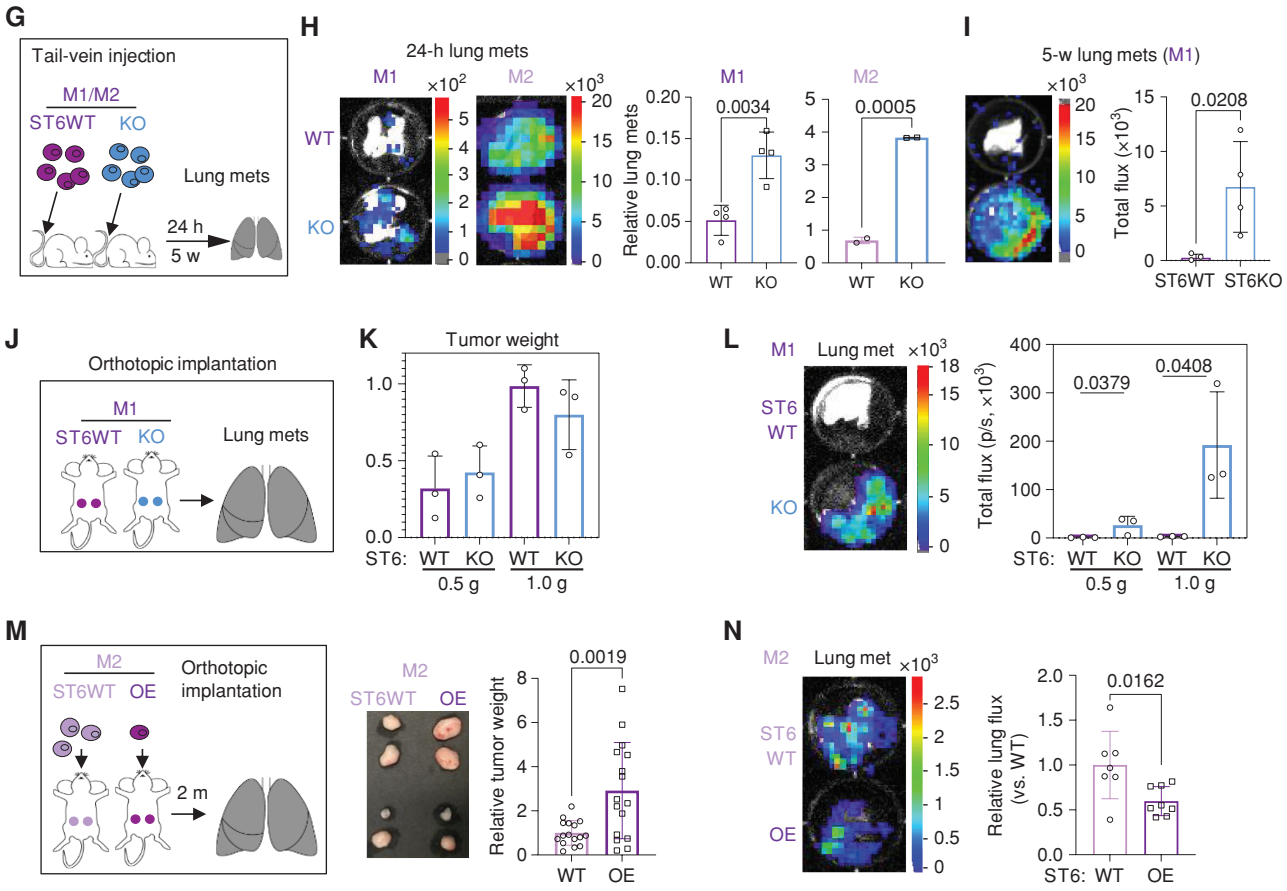

Figure 4. ***(Continued)*** **G,** Experimental illustration of tail-vein injection of ST6KO (KO) with appropriate ST6WT (WT) controls of PDX-M1 and PDX-M2 models; 1×10^5 cells/mouse were injected via tail vein, and lung localization signals were measured 24 hours and/or 5 weeks after injection. **H,** Representative images (left) and quantification (right) of lung metastatic seedings of ST6WT vs. ST6KO M1 and M2 models 24 hours after injection. Lung total flux of cellular bioluminescence signals was imaged prior to and after injections. **I,** Lung bioluminescence images (left) and quantified lung metastases (photons/s; right) 5 weeks after tail-vein injection of ST6WT and ST6KO cells. **J,** Schematic illustration of orthotopic implantations of ST6WT and ST6KO PDX-M1 into the fourth mouse mammary fat pads. Two batches of ST6WT (1.2×10^3 cells/injection) and ST6KO (5×10^3 cells/injection) cells were injected, and tumors were harvested when reaching ~0.5 g or 1.0 g. **K,** Quantified tumor weight for both ST6WT and ST6KO M1 tumors collected at various time points. **L,** Representative bioluminescence images (left) and quantified lung metastasis (right) of ST6WT and ST6KO PDX-M1 models at 0.5 g and 1.0 g, respectively. Data, mean ± SD of 8 experimental replicates. **M,** Schematic of orthotopic implantations of ST6WT (6×10^4 cells) and ST6OE (2×10^4 cells) PDX-M2 cells per mammary fat pad, photo of primary breast tumors, and tumor weight comparison between two groups to assess the lung metastases. **N,** Representative bioluminescence images of dissected lungs (left) and the relative lung metastases, presented as total flux of the lung bioluminescence, at 2 months of implantation. *P* values were calculated with Student *t* test using GraphPad, and data are represented as mean ± SD of 3–5 experimental replicates unless otherwise indicated.

After orthotopic implantations of ST6WT and ST6KO tumor cells in identical numbers, we observed a significant delay of tumor initiation and slower growth in ST6KO PDX tumors (both M1 and M2) in comparison with the WT controls (Supplementary Fig. S10A–S10C). When ST6WT M1 tumors reached ~1.0 g with significant dissemination, ST6KO M1 tumors at 0.2 g had almost undetectable metastases (Supplementary Fig. S10B), suggesting a minimal requirement of primary tumor volume for suitable evaluation of metastatic potential. Instead, ST6KO M2 tumors at 0.5 g seeded more spontaneous lung metastases relative to the tumor burden than the WT M2 tumors at the size of ~1.0 g (Supplementary Fig. S10B and S10C).

Furthermore, the ST6WT and ST6KO tumor cells in the PDX-M1 model were implanted at various ratios of cells or within extended time to reach relatively comparable tumor volumes (Fig. 4J and K). With matched tumor weight of 0.5 g or 1.0 g, α2,6-SA–deficient ST6KO M1 tumors developed >20-fold more spontaneous lung metastases than that of ST6WT M1 tumors (Fig. 4L–N). A higher number of CTCs and especially CTC clusters were detected in ST6KO M1 tumor-bearing mice than in the WT control via flow cytometry (Supplementary Fig. S10D–S10F).

Loss of ST6GAL1 Promotes Transendothelial Migration for Metastatic Seeding

To further assess the extravasation and metastatic seeding of SNA-low CTCs into the lungs, we performed endothelial CD31 staining with the lung tissue sections of PDX tumor-bearing mice to distinguish the vascular CTCs *in situ* and

extravascular DTCs (Supplementary Fig. S10G). In PDX-M1 tumor models, orthotopically implanted ST6KO tumors disseminated more DTCs to the lungs with a higher number of vascular CTC clusters than the ST6WT tumors but with relatively comparable single CTCs, detected via IHC staining of mouse lung sections (Supplementary Fig. S10G and S10H). In addition, ST6KO tumors disseminated more DTCs but showed a lower Ki-67 positivity than ST6WT cells (Supplementary Fig. S10I and S10J).

On the other hand, the metastatic potential of PDX-M2 models was assessed with ST6WT and ST6OE tumor cells implanted at a 3:1 ratio into separate mice (Fig. 4M). ST6OE M2 tumors with an upregulation of α2,6-SA levels grew into >2-fold higher tumor weight than the WT control tumors, but relatively impaired spontaneous lung metastasis, measured via bioluminescence imaging (Fig. 4N). IHC analyses further revealed that ST6OE decreased lesions and numbers of DTCs to the lungs, even with a relatively higher rate of Ki-67$^+$ DTCs than that of the ST6WT control tumors (Supplementary Fig. S11A–S11D).

We further evaluated the function of ST6GAL1 in transendothelial migration during metastatic seeding, using our established transendothelial migration assay (34, 35) with tumor cells seeded onto human umbilical vein endothelial cells (HUVEC; refs. 33, 34). Consistently, ST6KO MDA-MB-231 tumor cells with depleted α2,6-SA interacted with and transmigrated through HUVECs at a much higher efficiency than the ST6WT cells (Supplementary Fig. S12A). Similarly, within 24 hours following tail-vein injections, ST6KO (GFP) cells seeded in the lungs with a dramatically increased number of clusters than ST6WT (tdTomato) cells, in either separately injected or mixed injected (tdTomato-labeled ST6WT with eGFP-labeled ST6KO MDA-MB-231 cells; Supplementary Fig. S12B–S12F). In addition, following separate orthotopic implantations or mixed implantations into NOD/SCID gamma (NSG) mammary fat pads, ST6KO tumor cells seeded more colonies (total foci) into the lungs but developed into smaller lung colonies compared with ST6WT tumor cells (Supplementary Fig. S12G–S12L) due to a relatively quiescent phenotype of ST6KO tumor cells (Figs. 3 and 4; Supplementary Figs. S10 and S11).

Together, these results demonstrate double-edge regulatory effects of ST6GAL1, deficiency of which slows down tumor growth but improves CTC clustering and subsequent seeding into the lungs, whereas ST6GAL1 upregulation enhances tumor growth with compromised dissemination and metastasis. However, the dynamics of ST6GAL1 alteration with its transient deficiency in CTCs enables clustering and seeding as rate-limiting steps, whereas restored expression in DTCs empowers secondary regeneration rates in mice.

Glycoproteomic Analyses Reveal Novel α2,6-Sialylation Substrates of ST6GAL1

To identify the glycoprotein targets of ST6GAL1 that impact tumor cell cluster formation and metastatic seeding, we performed global glycoproteomic analysis of SNA-precipitated proteins from the membrane fractions or whole-cell lysates of ST6WT and ST6KO cells (MDA-MB-231; Fig. 5A). A total of 217 SNA-bound glycoproteins were specifically identified from the membrane fractions of ST6WT cells in comparison with the negative control of ST6KO cells, including previously known proteins that facilitate CTC cluster formation such as CD44 (4), EGFR (36), ICAM1 (15), and Desmoglein 2 (DSG2; ref. 37; Supplementary Excel S4; Supplementary Fig. S13A). Among these glycoprotein targets of ST6GAL1, 68 peptides with characterized N-linked glycans belong to 14 glycoproteins, including known targets of ST6GAL1 (integrin β1) and many newly identified targets such as adhesion molecules PODXL, CD97, ECE1, ALCAM1, and ICAM1, immune regulator HLA-A2, and exosomal proteins CD63, LAMP1, and LAMP2 (Fig. 5B; Supplementary Excel S5). Immunoblotting of the SNA precipitates further confirmed that PODXL, CD97, ECE1, ALCAM1, ICAM1, and CD44 were enriched in the membrane fractions and specifically pulled down by SNA from WT cells only (Fig. 5C; Supplementary Fig. S13B).

We hypothesized that these adhesion glycoproteins contribute to tumor cell cluster formation and metastatic seeding, and their levels and/or activity are subject to and regulated by ST6GAL1-mediated sialylation. To examine the importance of unknown adhesion glycoproteins in cluster formation, we transfected both ST6WT and KO cells with siRNAs to deplete individual target proteins. Using ICAM1 and DSG2 knockdown as positive controls, downregulation of PODXL, CD97, ECE1, and ALCAM1 also significantly inhibited cluster formation of ST6KO cancer cells, in which PODXL knockdown particularly reversed the clustering level equivalent to the ST6WT cells (Fig. 5D–F; Supplementary Videos S8–S14). Moreover, the knockdown of PODXL and other adhesion molecules in ST6WT cells also slightly suppressed the tumor cell cluster formation except for ALCAM1 and DSG2, which had minimal effects (Supplementary Fig. S14A–S14C; Supplementary Videos S15–S20). These data demonstrate that targeting of the downstream adhesion molecules of ST6GAL1 provides possible strategies to partially or completely reverse the tumor cell clustering promoted by the loss of α2,6-SA or ST6GAL1.

We continued to analyze the expression of adhesion molecules in the CTCs of patients with breast cancer using CellSearch and flow cytometry. PODXL expression was significantly enriched in the CTC clusters in comparison with single CTCs isolated from the blood of patients with breast cancer (Fig. 5G). An increased protein expression level of PODXL was also observed in ST6KO cells without an alteration of mRNA expression (Supplementary Fig. S14D and S14E), implicating the potential posttranslational advantages of desialylated PODXL. Furthermore, we isolated sialylated and desialylated PODXL protein from respective ST6WT and ST6KO cell membrane fractions for cellular binding. The dP-KO binding between desialylated PODXL (dP) and ST6KO cells was stronger than other pairs of bindings, such as dP-WT (dP binding with ST6WT cells) and P-KO (sialylated PODXL binding with ST6KO cells; Fig. 5H). Consistently, after NA treatment, desialylated CD44 increased binding affinity for its homophilic interactions on solid phase (Supplementary Fig. S14F). This suggests that ST6GAL1-mediated α2,6-sialylation of PODXL may negatively regulate protein stability and/or inhibit their binding activity necessary for tumor cluster formation. The molecular mechanism

A

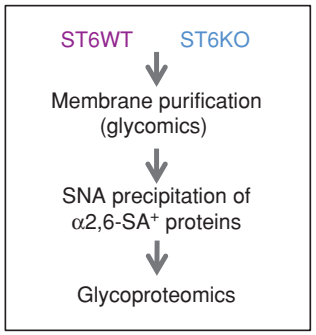

B

Name	Sequence	Glycans
PODXL	K.QLVLN[+2350.83035]LTGNTLC[+57.02146]AGGASDEK.L	HexNAc(4)Hex(5)Fuc(1)NeuAc(2)
ECE1	R.FFN[+1913.67702]FSWR.V	HexNAc(4)Hex(5)NeuAc(1)
CD97	R.LSAVNSIFLSHN[+2059.73493]NTK.E	HexNAc(4)Hex(5)Fuc(1)NeuAc(1)
ALCAM1	R.N[+2407.85181]ATVVWMK.D	HexNAc(5)Hex(5)NeuAc(2)
ICAM1	K.N[+3155.13152]LTLR.C	HexNAc(7)Hex(8)Fuc(1)NeuAc(1)

C

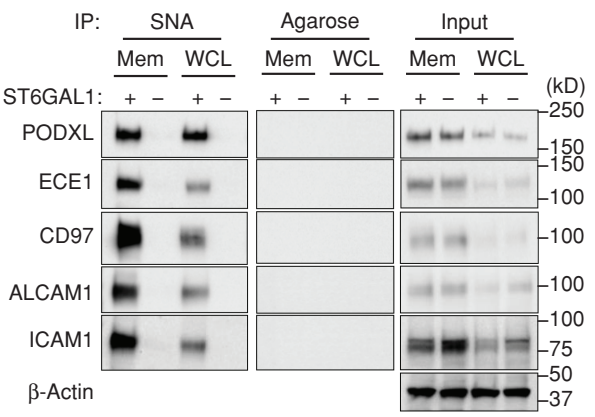

D

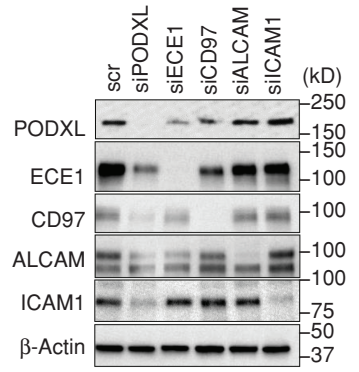

E

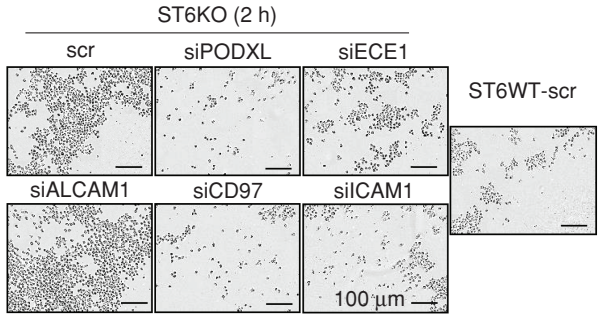

F

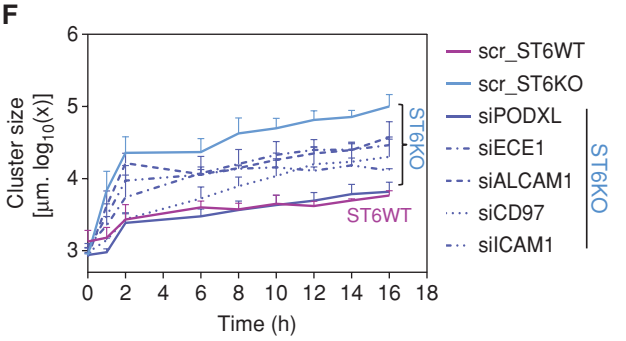

G

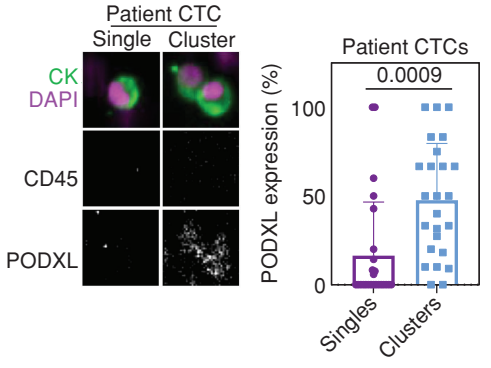

H

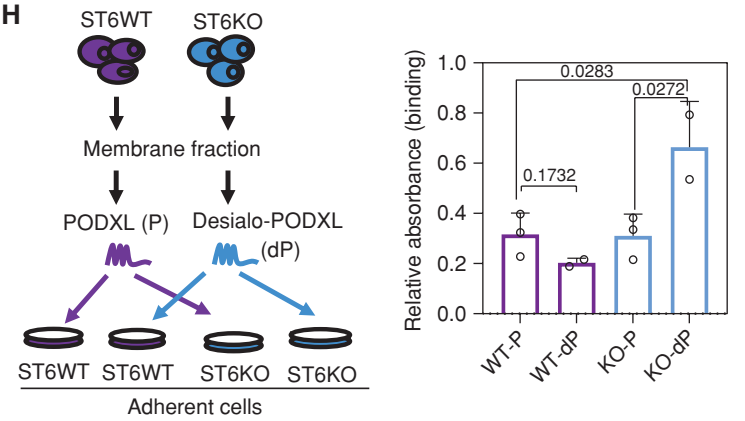

of ST6GAL1-mediated stability of PODXL remains in our future investigation.

Targeting PODXL Blocks Lung Metastasis Promoted by ST6GAL1 Deficiency and Chemoevasion

To demonstrate whether PODXL and other adhesion molecules contribute to ST6GAL1 deficiency–promoted metastatic seeding *in vivo*, we knocked down these genes in ST6KO and ST6WT cells prior to cell inoculation into mice. Reduced expression levels of PODXL, CD97, ECE1, ALCAM1, and ICAM1 in these tumor cells were verified via immunoblotting (Fig. 5D; Supplementary Fig. S14A). At 24 hours after tail-vein injection, PODXL knockdown effectively blocked 80% to 90% of metastatic seeding and tumor cluster formation in both ST6KO and ST6WT cells (Fig. 6A–C), similar to the inhibitory effects of ICAM1 knockdown (4, 15), whereas knockdown of ECE1, CD97, and ALCAM1 displayed relatively weaker inhibitory effects (Supplementary Fig. S15A–S15F). PODXL knockdown had minimal effects on the proliferation or the viability of transfected cells (Supplementary Fig. S15G and S15H). Similarly, cell viability was not affected by CD97 knockdown and was slightly improved by knockdown of ECE1 or ALCAM1 except for a small decrease by ICAM1 downregulation (Supplementary Fig. S15H).

As a proof of concept, we investigated the possibility of targeting PODXL therapeutically using a neutralizing antibody in multiple tumor models. Administration with the anti-PODXL antibody (5–20 μg/mL) significantly blocked tumor cell cluster formation of ST6KO and ST6WT tumor cells (MDA-MB-231), as well as the M2 PDX cells *ex vivo* (Supplementary Fig. S16A–S16C). Knockdown of PODXL diminished the binding of anti-PODXL to these cells, suggesting minimal off-target binding of this antibody to PODXL-negative cells (Supplementary Fig. S16D). When anti-PODXL antibody was administered intravenously once (7 μg/mouse) at 1 hour prior to tumor cell inoculation, it efficiently blocked nearly half of the metastatic seeding from both ST6WT and ST6KO MDA-MB-231 tumor cells as measured 24 hours after tail-vein inoculation (Fig. 6D–F; Supplementary Fig. S16E and S16F).

We then tested the efficacy of anti-PODXL in preventing and treating the metastatic PDX models (M1 and CTC-092), which resist PAX chemotherapy. In an experimental metastasis study, the dissociated ST6WT PDX tumor cells were pretreated with PAX (50 μg/mL) *ex vivo* for 12 hours and then inoculated via tail vein into the mice. Mice were pretreated with PAX (27 mg/kg) 3 hours prior to cell inoculation (Fig. 6G). Revealed by the analyses at 20 hours and 3 weeks, PAX-promoted metastatic seeding of these tumor cells to the lungs was almost completely inhibited by concurrent treatment with anti-PODXL (20 μg/mL *ex vivo* and 30 μg/mouse via intravenous injection) in M1 PDX models (Fig. 6G–I). In CTC-092 PDX models, anti-PODXL administration also reduced lung colonization in both PBS and PAX treatment groups (Supplementary Fig. S17A).

We further investigated the therapeutic effects of anti-PODXL on spontaneous metastasis that is elevated by ST6KO and PAX treatment in PDX tumor cells (Fig. 6I). Following orthotopic tumor implantations, the PAX administration (13.5 mg/kg, i.p., every 3 days for 11 cycles, started from the second week) failed to shrink the primary tumor but increased spontaneous lung metastases along with elevated CTC clusters (Fig. 6J–N). Intravenous anti-PODXL treatment at the dosage of 20 μg/mouse concurrent to PAX treatment (every 3 days for 11 cycles) effectively blocked spontaneous metastases along with a dramatic reduction in CTC clusters (Fig. 6N; Supplementary Fig. S17B–S17E).

In summary, our work reports PODXL as a promising new target of ST6GAL1, contributing to the increased formation of quiescent CTC clusters and breast cancer metastasis in response to PAX therapy.

DISCUSSION

Collectively, our study demonstrates that PAX-induced loss of ST6GAL1 and α2,6-sialylation promotes adhesion molecule–mediated CTC cluster formation and metastatic seeding of TNBC. During chemotherapeutic treatment, the prognosis of TNBC is determined not only by treatment response in the primary tumor but also by the metastatic outgrowth. Chemoevasion is one of the most challenging problems compromising patient survival. PAX has previously been shown to delay tumor growth but increase metastasis with unknown mechanisms (38). Our study unveils the unexpected effects of chemoevasion and ST6GAL1 deficiency on promoting CTC cluster formation linked to an expected quiescence phenotype. A number of studies have also shown

Figure 5. Glycoproteomic analyses reveal novel α2,6-sialylation targets of ST6GAL1. **A,** Experimental design of glycoproteome profiles of SNA-bound α2,6-SA$^+$ membrane proteins isolated from ST6WT and KO cells. The membrane fractions were isolated, and α2,6-SA–linked proteins were coimmunoprecipitated with SNA-conjugated agarose beads. Purified proteins were loaded to the glycoproteomics analysis. **B,** The list of top ST6GAL1 target glycoproteins including their α2,6-sialylation sites on the peptide. **C,** Immunoblots of the ST6GAL1 substrates PODXL, ECE1, CD97, ALCAM1, and ICAM1 with immunoprecipitation (IP) by SNA (α-2,6-SA$^+$ proteins) or agarose controls, and input controls of the membrane fraction (Mem) or whole-cell lysate (WCL) from ST6WT (+) and ST6KO (–) MDA-MB-231 cells. **D,** Immunoblots of ST6GAL1 target proteins and the loading control β-actin from the lysates of ST6KO MDA-MB-231 cells transfected with the scramble control (scr) and siRNAs for PODXL, ECE1, CD97, ALCAM1, and ICAM1. **E** and **F,** Representative images of clusters at 2 hours (**E**) and cluster formation curves over the time (0–16 hours; **F**) of ST6KO MDA-MB-231 cells after downregulation of indicated genes. P scrST6KO vs. WT < 0.0001, P scrST6KO vs. siPODXL = 0.0001, P scrST6KO vs. siECE1 = 0.0175, P scrST6KO vs. siALCAM1 = 0.0260, P scrST6KO vs. siCD97 = 0.0043, and P scrST6KO vs. siICAM1 = 0.0003; scale bars = 100 μm. *P* values were calculated with the *t* test using GraphPad. Data are represented as mean ± SD of 12 experimental replicates. Cluster videos are available as Supplementary Videos S8–S14. **G,** Representative images of PODXL staining on patient CTCs (CD45$^-$CK$^+$DAPI$^+$) via CellSearch (left) and flow cytometry–based quantification (right) of PODXL expression. **H,** Schematic (left) and quantification (right) of cell-binding analyses (ST6WT/ST6KO) with PODXL and α2,6-desialylated PODXL isolated from ST6WT and ST6KO cells, respectively. *P* values were calculated with the Student *t* test using GraphPad, and data are represented as mean ± SD of 3–5 experimental replicates unless otherwise indicated.

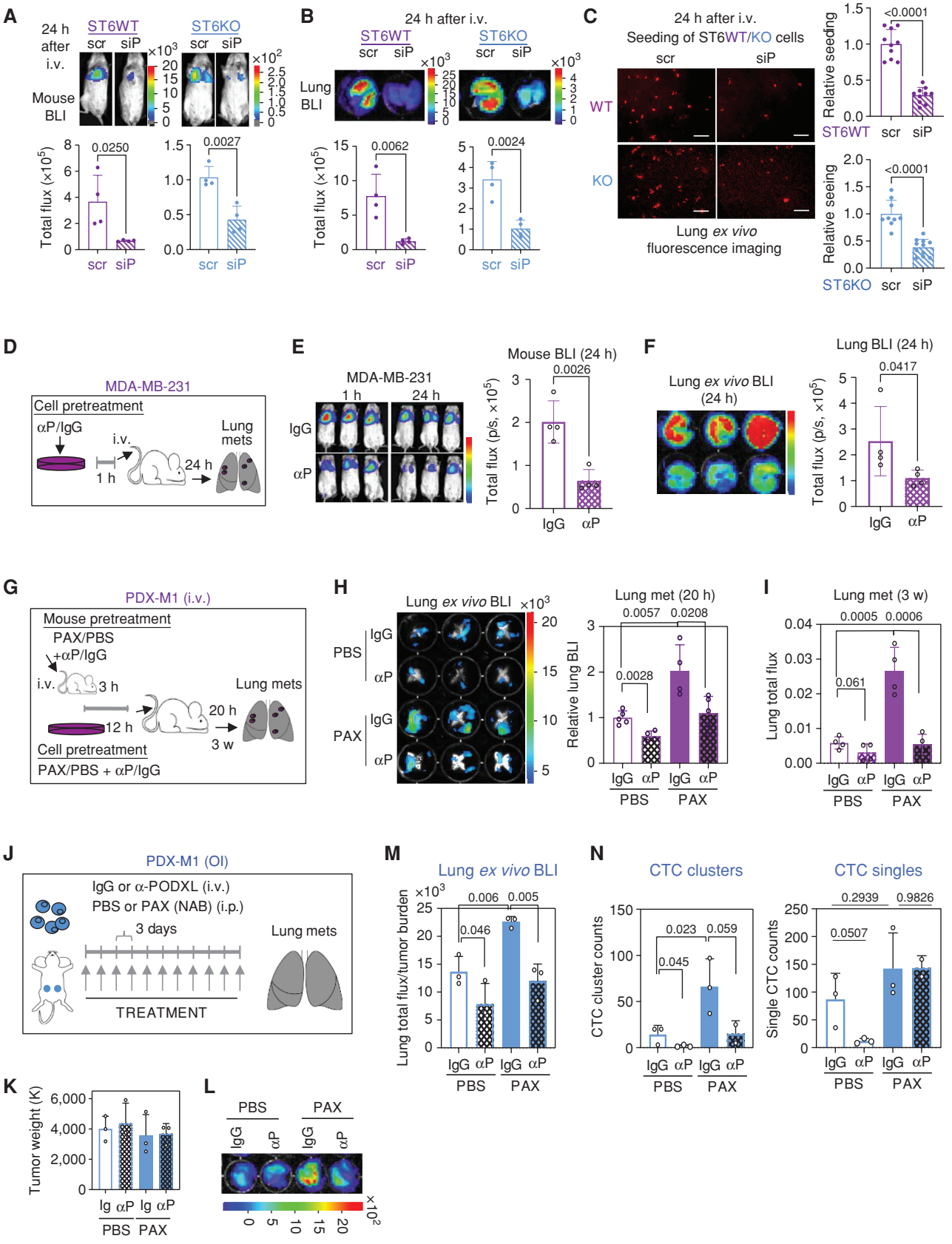
A
24 h after i.v.
ST6WT
ST6KO
scr siP
Mouse BLI
Total flux (×10^5)
0.0250
0.0027
B
24 h after i.v.
Lung BLI
0.0062
0.0024
C
24 h after i.v.
Seeding of ST6WT/KO cells
WT
KO
Lung ex vivo fluorescence imaging
Relative seeding
<0.0001
D
MDA-MB-231
Cell pretreatment
αP/IgG
i.v.
1 h
24 h
Lung mets
E
MDA-MB-231
1 h 24 h
IgG
αP
Mouse BLI (24 h)
0.0026
F
Lung ex vivo BLI (24 h)
0.0417
G
PDX-M1 (i.v.)
Mouse pretreatment
PAX/PBS +αP/IgG
3 h
12 h
20 h
3 w
Cell pretreatment
PAX/PBS + αP/IgG
H
Lung ex vivo BLI
PBS
PAX
Lung met (20 h)
0.0057
0.0208
0.0028
Relative lung BLI
I
Lung met (3 w)
0.0005
0.0006
0.061
Lung total flux
J
PDX-M1 (OI)
IgG or α-PODXL (i.v.)
PBS or PAX (NAB) (i.p.)
3 days
TREATMENT
Lung mets
K
Tumor weight (K)
L
M
Lung ex vivo BLI
0.006
0.005
0.046
Lung total flux/tumor burden
N
CTC clusters
0.023
0.059
0.045
CTC cluster counts
CTC singles
0.2939
0.9826
0.0507
Single CTC counts

that PAX induces drug resistance through NF-κB activation and tumor cell dissemination by activating inflammation that promotes angiogenesis (39). PAX may also induce breast cancer cell intravasation and dissemination by promoting the formation of a microanatomic structure called tumor microenvironment of metastasis (known as TMEM; ref. 38). Interestingly, our signaling pathway analysis also reports that loss of ST6GAL1 results in activation of tumor-intrinsic inflammatory pathways that may also relate to chemoevasion and the responses in PAX-treated cells.

Targeting quiescent metastatic stem cells and/or CTC clusters is a demanding task to counter chemoevasion and block metastasis. The comprehensive glycoproteomic analysis of α2,6-sialylated proteins provides a robust platform by which we have further identified new adhesion protein substrates of ST6GAL1, such as PODXL, as innovative therapeutic targets. In addition to promoting homotypic CTC–CTC cluster formation, ST6GAL1 deficiency also promotes heterotypic tumor cell–endothelial cell interactions, thereby facilitating transendothelial migration, which is a gatekeeping step during metastatic seeding. Antibody-mediated blockade of PODXL interaction with neighboring cells further suggests a proof-of-concept therapeutic approach for inhibiting CTC cluster formation and blocking lung metastasis of TNBC.

Although PODXL is one of the top substrates responsible for ST6GAL1-mediated regulation in metastatic seeding, many others may be required for optimal tumor stem cell cluster formation, such as ICAM1 (15), CD44 (4), and EGFR (36), as demonstrated in our previous studies. Moreover, large CTC clusters may also be trapped in capillaries or enable closure of such vasculatures for initiation of colonization (16). Seeking combinational targeting approaches to prevent and treat metastasis remains urgent and to be further advanced.

Glycosylation of cell-surface proteins is constantly and dynamically changing and is associated with cancer development (18) in a context-dependent manner in various cancers, including breast (21), prostate (40), ovarian (41), and colorectal cancers (42, 43). Glycosylation patterns modulate cell-surface polarity and protein binding affinity to finely tune cell–cell and protein–protein interactions (18). Altered glycosyltransferases and glycosylation are often associated with oncogenic transformation in various cancers, including breast cancer. The most frequent altered glycosylations are sialylation, fucosylation, and O-glycan truncation (18, 19). N-glycan sialylation refers to the covalent addition of negatively-charged SAs via α2,3-, α2,6-, or α2,8-bonds to the terminal end of oligosaccharides that are linked to the asparagine (N) residue of glycoproteins (20).

Although sialylation may increase intercellular communication via lectin ligand–binding activities of glycoproteins (18, 19), loss of α2,6-sialylation promotes CTC cluster formation and metastatic seeding, likely through enhanced binding of ST6GAL1 substrate adhesion molecules. In addition to investigating a possible negative association between CD44 and ST6GAL1, future studies will be pursued to elucidate the biochemical properties and regulatory mechanisms underlying transient and dynamic loss of α2,6-sialylation in CTCs during metastasis and in response to chemotherapy. We speculate that the negative charges α2,6-SA brings to glycoproteins on cell surfaces may cause cell repulsion and shedding of migratory tumor cells at the early steps of metastasis, and removal of α2,6-SA in CTCs may expose strong binding sites among cell adhesion molecule and their ligands to facilitate clustering and seeding with advantageous quiescence to evade chemotherapy. In mammals, α2,6-sialylation is catalyzed by two different sialyltransferases, ST6GAL1 and ST6GAL2 (21). Although ST6GAL1 is ubiquitously expressed in human tissues and implicated in various tumors, including breast cancer, ST6GAL2 expression is limited to the brain cortex and embryos (21). It might be interesting to examine if chemotherapy or PAX impacts ST6GAL2 and cellular functions in those tissues, such as neuropathy.

METHODS

Human Specimen Analyses

All human specimen collection and blood sample analyses were performed according to Northwestern University's IRB-approved protocol (IRB STU00203283) and following NIH guidelines for human subject studies. Written informed consent was provided by the patients whose blood and/or tissue specimens were analyzed for the study.

OS Analysis

The cohort consisted of 157 patients with metastatic breast cancer longitudinally characterized for CTCs and CTC clusters at the Robert H. Lurie Comprehensive Cancer Center at Northwestern University (Chicago, IL). Patients were enrolled under the Investigator Initiated Trial NU16B06 (IRB STU00203283) at the time of initial metastasis

Figure 6. Targeting PODXL blocks ST6KO- and chemo-associated metastasis. **A–C,** Bioluminescence images (BLI) and lung metastasis quantifications of mouse imaging (**A**) and dissected lungs *ex vivo* (**B**), and fluorescence images and relative metastatic seeding (disseminated colonies) to the lungs (**C**) 24 hours after tail-vein injections of ST6WT (in purple) and ST6KO (in blue) cells transfected twice with scrambled control (scr) and siPODXL (siP) for gene knockdown. Scale bars = 100 μm. **D–F,** Experimental design (**D**), as well as representative images and quantification of mouse BLI (**E**) and lung *ex vivo* BLI (**F**) to determine the lung metastases (met) after administration of IgG and anti-PODXL (αP) neutralizing antibody to ST6WT MDA-MB-231 cells [6.5×10^4 cells/mice were preincubated with αP antibody (7 μg/mice) or isotope control IgG (7 μg/mice) for 1 hour]. Cells were then injected via the tail vein, and bioluminescence imaging was measured after 24 hours of injection (**E**). Then mice were sacrificed and *ex vivo* images of the lungs were measured (**F**). **G,** Schematic view of experiment for cotreatment of PAX and αP antibody, PDX-M1 tumor cells were pretreated with PAX-NAB (50 μg/mL) or PBS with αP (20 μg/mL) or IgG control (20 μg/mL) and incubated for 12 hours at 37°C. Meanwhile, mice were treated with the same combination of drugs (PAX-NAB, 27 mg/kg or PBS, αP or IgG control, 30 μg/mouse) via tail vein 3 hours prior to cell inoculation. Twenty hours and 3 weeks (3 w) after i.v. injection of the cells, lungs were dissected for *ex vivo* bioluminescence imaging (**H**, left, 20 hours) and disseminated lung metastasis quantified as total flux in **H** (right, 20 hours) and **I** (3 w). **J–N,** Experimental design of cotreatment of mice bearing orthotropic (OI) PDX-M1 tumors. First, ST6KO M1-PDX cells were injected into a mammary fat pad. Mice were cotreated with PAX-NAB (13.5 mg/kg) or PBS and αP or IgG control (20 μg/mouse) once every 3 days. After 11 times treatments, mice were sacrificed for further analysis. Tumor weight (**K**), representative images of lung bioluminescence imaging (**L**) with normalized quantification of lung total flux with tumor weight (**M**), and the count of CTC clusters (**N**; left) and single CTCs (right) are shown. *P* values were calculated with the Student *t* test using GraphPad. Data, mean ± SD of 3–4 biological replicates.

or disease progression, independent of line of therapy. Imaging was performed according to the investigators' choice. Cluster enumeration was performed before treatment started (baseline) and at the first clinical evaluation one (E1) within a median of 3 months after the baseline time point. OS was defined as the time from baseline until any cause. Patients without an endpoint event at the last follow-up visit were censored. Differences were analyzed by the log-rank test and presented by Kaplan–Meier estimator plot.

Animal Studies

PDX mouse models were kept in specific pathogen–free facilities in the Animal Resources Center at Northwestern University. All animal procedures complied with the NIH Guidelines for the Care and Use of Laboratory Animals and were approved by the Northwestern University Institutional Animal Care and Use Committee (IACUC protocol IS00016125). Animals were randomized by age. Sample sizes were specified based on the results of preliminary experiments. Immunodeficient NSG mice (8–10 weeks old) were utilized for orthotopic implantation and tail-vein injection of multiple TNBC PDX models and MDA-MB-231 breast cancer cell lines. The PDX models were established as described previously (8).

CTC Analyses by CellSearch and Flow Cytometry

Two complementary methods were previously established in the laboratory for CTC analyses in parallel using distinct blood sample tubes (4, 44). One is the FDA-approved CellSearch platform, with blood drawn directly into CellSave Preservative Tubes (Menarini Silicon Biosystems), which contain cell preservatives to keep CTCs intact under storage at room temperature. Another is flow cytometry of live CTCs (blood cell lineage–negative) with blood drawn into EDTA Vacutainer tubes (Becton Dickinson).

CellSearch. The CellSearch System (Menarini Silicon Biosystems) is semiautomated for blood sample processing, enrichment of $EpCAM^+$ epithelial CTCs using the Epithelial Cell Kit (EpCAM-coated magnetic beads), and subsequent four-channel immunofluorescence staining as described by Cristofanilli and colleagues (44). Normally, CTCs are specified by combining three routine channels of DAPI positivity, negative for the white blood cell marker CD45, and positive for the epithelial marker CK (8, 18, 19), with the fourth and the only channel open for analysis of one customized candidate marker, such as glycans and proteins. Fluorophore-labeled lectins were used for glycan recognition, such as Flourescein-labeled Sambucus Nigra Lectin (SNA, EBL; Vector Laboratories, FL-1301) for α2,6-SA analysis. Fluorophore-conjugated antibodies were chosen for optimized detection of proteins, such as anti-PODXL (Santa Cruz Biotechnology, 3D3, sc-23904 PE) and anti–Ki-67 (Abcam, SP6, ab282173). For the PODXL staining, blood samples were prestained with antibody for 30 minutes at 37°C and then proceeded for semiautomated processing on CellSearch as described (44, 45).

Flow Cytometry. The protocol of flow cytometry for CTC analysis was previously established (4) and optimized for comprehensive analysis of glycans and other protein markers. The blood samples were collected into EDTA Vacutainer tubes (Becton Dickinson) from patients with breast cancer and stored on ice or at 4°C temporarily prior to manual blood processing within 24 hours. After multiple rounds (two to four rounds) of red blood cell lysis (lysis buffer, Sigma, R7757), white blood cells (mainly peripheral blood mononuclear cells) were washed twice with PBS. Cells were fixed with 3% paraformaldehyde for 30 minutes for glycan and protein profiling analyses. Cells were blocked with carbo-free blocking solution (Vector Laboratories, SP-5040) and stained with antibodies for proteins (CD45, epithelial marker EpCAM, and other blood cell lineage markers) and lectins for glycans, such as SNA-FITC, MALII-FITC, PHA-L-PE, LTL-FITC, RCA-Rho, LEL-APC, ConA-PE (Vector Laboratories), and MALII-FITC (GlycoMATRIX). CTCs were gated based on cell size (forward-scatter and side-scatter channels), CD45 negativity, and $EpCAM^{+/-}$ $CK^{+/-}$.

Cell Lines and Transfections

Human MDA-MB-231 cells and mouse breast cancer cell line 4T1 were purchased commercially from ATCC and periodically verified to be *Mycoplasma*-negative using the MycoAlert Mycoplasma Detection Kit (Lonza, LT07-218). Cell morphology, growth characteristics, and microarray gene expression analyses were compared with published information to ensure their authenticity. Early passage of cells (<15 passages) was maintained in Dulbecco's modified Eagle medium with 10% fetal bovine serum (FBS) plus 1% penicillin–streptomycin (P/S). Primary tumor cells were cultured in HuMEC-ready medium (Life Technologies) plus 5% FBS and 0.5% P/S in collagen type I (BD Biosciences)–coated plates. ON-TARGETplus siRNAs for ST6GAL1, PODXL, ALCAM1, ECE1, CD97, and ICAM1 and nontargeting control siRNA were purchased from Dharmacon and transfected using Dharmafect (Dharmacon) at 50 nmol/L; for the double knockdown, cells were transfected again after 24 to 48 hours. Transfection efficiency was evaluated by flow cytometry analysis and Western blotting.

Tumor Dissociation and Orthotopic Injection

L2T- or L2G-labeled PDX tumors or MDA-MB-231 cell tumors were dissociated with liberase TH lysis buffer (Sigma-Aldrich) according to the supplied protocol, and after dissociation, cells were filtered with 70-μm and 40-μm strainers. Red blood cells were lysed with red blood cell lysing buffer (Sigma) for 1 minute on ice and washed with PBS. Next, 100 to 1,000 cells were resuspended in Matrigel:phosphate-buffered saline (PBS; 50:50 μL) and injected under the mammary fad pad. Tumor growth was monitored weekly under *in vivo* bioluminescence imaging (see below). After mice were euthanized, tumors were dissected and weighed and dissociated for clustering assays, Western blotting, and flow cytometry analysis. Lung metastases were imaged by fluorescence microscopy and bioluminescence imaging and fixed with 4% paraformaldehyde for immunofluorescence staining and 4% formalin for IHC. Lungs were dissociated using the same techniques as tumors for flow cytometry analysis to quantify lung metastasized cells.

Tail-Vein Injection

After dissociation of the tumors, L2G- or L2T-labeled PDX cells (0.5×10^5 – 2×10^5/mouse) or MDA-MB231 cells (1×10^5/mouse) were resuspended in PBS (200 μL/mouse) and reinjected via the tail vein. Because the bioluminescence signal is dependent on cellular metabolic energy and modulation of the *ST6GAL1* gene affects cellular activity, the same number of cells per mouse was imaged by bioluminescence before injection to estimate lung localization of the cells. Mice were imaged right after tail-vein injection and 24 hours after injection. After that, mice were euthanized and lung metastasis was measured by bioluminescence imaging and fluorescence microscopy. Lungs were dissociated for flow cytometry analysis and fixed for immunofluorescence and IHC analysis.

PAX Treatment of M1-PDX Model after Orthotopic Inoculation

ST6WT cells (1×10^6) were injected into a mammary fad pad. After 1 week of tumor growth, mice were treated with PAX-NAB (13.5 mg/kg) or PBS control (every 3 days, 10 times). Mice were sacrificed, and blood was collected from the heart individually. Red blood cells were lysed by using RBC buffer (0.15 M ammonium chloride, 1 mmol/L potasium bicarbonate, 0.1 mmol/L EDTA, pH 7.2–7.4). tdTomato-labeled PDX-M1 CTCs in blood and the percentage of SNA-high and Ki-67 staining in single CTCs and CTC clusters were quantified using flow cytometry. The gating strategy of CTCs is shown in

Supplementary Fig. S17. After collecting blood, tumor and lungs were dissected and lung *ex vivo* bioluminescence imaging was measured as explained above.

Anti-PODXL Antibody Treatment of MDA-MB-231 Tumor Cells via Tail-Vein Injection

ST6WT and ST6KO cells (6.5×10^4) were pretreated with 7 μg/mouse concentration of antibody or isotope IgG control for 2 hours at 37°C. Cells in 200 μL were then inoculated directly to the mice via the tail vein. Because bioluminescence imaging of the ST6WT and ST6KO cells was different due to cell activity, we first performed bioluminescence imaging of the same number of cells for further analyses. After cell inoculation, bioluminescence imaging of the mice was performed after 1 hour and 24 hours and then the mice were sacrificed. Lung *ex vivo* images were taken right after the sacrifice. The quantifications of the total fluxes were normalized with the total flux of the cells that were imaged before cell tail-vein injection.

Anti-PODXL and PAX-NAB Treatment of M1-PDX/CTC-092-PDX via Tail-Vein Injection

Luc2-tdTomato-labeled PDX-M1 or CTC-092-PDX cells were dissociated and pretreated with PAX-NAB (50 μg/mL) and/or anti-PODXL antibody or isotope control IgG (20 μg/mL) for 12 hours. After washing and centrifugation, 5×10^5 cells were inoculated into the tail vein of the mice pretreated with PAX (27 mg/kg) and anti-PODXL or IgG (~30 μg/mouse) 3 hours prior to cell inoculation. Twenty hours or 3 weeks after tumor cell injections, bioluminescence signals of the mice and dissected lungs were imaged using SII LAGO (excitation wavelength was 465 nm and emission filter wavelength was 510 nm).

Cotreatment of Anti-PODXL and PAX in M1-PDX after Orthotopic Inoculation

ST6KO cells (1×10^6) were injected into a mammary fad pad. After 1 week of tumor growth, mice were treated with PAX-NAB (13.5 mg/kg) and/or anti-PODXL antibody or isotope control IgG (10 μg/mouse, every 3 days, 12 times). Mice were sacrificed, and blood was collected from the heart individually. Red blood cells were lysed using RBC buffer (0.15 M ammonium chloride, 1 mmol/L potassium bicarbonate, 0.1 mmol/L EDTA, pH 7.2–7.4). tdTomato-labeled PDX-M1 CTCs in blood were quantified using flow cytometry. The gating strategy is shown in Supplementary Fig. S14. After blood collection, tumor and lungs were dissected and lung *ex vivo* bioluminescence imaging was measured as explained above. The total flux of lungs was normalized with tumor weight.

Bioluminescence Imaging

After intraperitoneal injections with 100 μL of D-luciferin (30 mg/mL, Gold Biotechnology, 115144-35-9), mice were anesthetized with isoflurane. Bioluminescence images were acquired using a Spectral Lago system from Spectral Instruments Imaging, and the signals are presented as total flux (photons/second, p/s) and fold changes of the total flux signals (Aura, version 2.2.1.1). Acquisition times ranged from 5 seconds to 5 minutes.

Flow Cytometry and Cell Sorting

L2T- or L2G-labeled PDX tumor cells or MDA-MB-231 cells were washed twice with PBS and blocked with carbo-free blocking solution (Vector Laboratories, SP-5040) for 20 minutes on ice (1×10^6 cells in 0.2 mL). Then cells were incubated with the appropriate lectins (1 μL/1×10^6 cells), including biotinylated SNA, MAL-II, LTL, or PHA-L (Vector Laboratories). Streptavidin-labeled APC antibodies were used as secondary antibodies at the beginning of the experiments, and later SNA-FITC and SNA-APC (Vector Laboratories) were used at the same concentrations. CD44 antibody with PE, APC, FITC, or Pe-Cy7 labels (R&D Systems) was coincubated with lectins at the concentrations suggested by the manufacturers. Cells were analyzed with a BD-LSR II flow cytometer (BD Biosciences) or a BDAria cell sorter (BD Biosciences). DAPI was used for cell viability control.

Western Blotting and Immunoprecipitation

Cultured cells were scraped and washed twice with PBS before lysing with RIPA buffer (Thermo Fisher) with protease inhibitor cocktail (1:100 dilution, Thermo Fisher). Lysis was completed for 30 minutes on ice, and the mixture was centrifuged for 10 minutes at 4°C and 14,000 rpm. For Western blotting, 2 to 10 μg of protein was denatured at 100°C for 5 minutes and subjected to SDS-PAGE and then transferred to PVDF membranes. For immunoprecipitation, 100 to 1,000 μg of protein was first preincubated with agarose beads (Vector Laboratories) for 1 hour. Then SNA-tagged agarose beads (Vector Laboratories, Al-1303) were added to the lysates and incubated overnight at 4°C on a rotator. SNA-bound proteins were eluted with SDS buffer (Bio-Rad) and subjected to SDS-PAGE. Antibodies against ST6GAL1 (R&D Systems, AF5924), ST3GAL1 (R&D Systems, AF6905-SP), FUT3 (I; anti-CD174, BioLegend, 392602), FUT3 (II; Abcam, ab110082), CERCAM (Santa Cruz Biotechnology, D-4, sc-514083), Serpine-1 (Proteintech, 13801-1-AP), L1CAM (Thermo Fisher, 1.G11B1, MA526429), CD44 (Thermo Fisher, 8E2F3, MA515462), PODXL (Santa Cruz Biotechnology, 3D3, sc-23904), ICAM1 (Sigma, HPA004877), ECE1 (Santa Cruz Biotechnology, A-6, sc-376017), ALCAM1 (Proteintech, 21972-1-AP), CD97 (Santa Cruz Biotechnology, G-8, sc-166852), Na+/K+ ATPase aptha1 (Santa Cruz Biotechnology, C464.6), and β-actin (Sigma, A5441) were used as primary antibodies, and horseradish peroxidase (HRP)–conjugated secondary antibodies were from Promega (Rabbit W401B and Mouse W402B). The substrate ECL was detected by Pierce ECL2 solution (Thermo Fisher Scientific, 1896433A).

Release of N-linked Glycans from Cells

About 20×10^6 cells were lysed in a high-salt buffer (2M NaCl, 5 mmol/L EDTA in 100 mmol/L Tris-HCl, pH 7.5) and centrifuged at 15,000 rcf for 5 minutes, and the pellet was collected. The protein pellet was subsequently dissolved in a urea lysis buffer (8 mol/L urea, 4% CHAPS, 100 mmol/L DTT, 5 mmol/L EDTA in 100 mmol/L Tris-HCl, pH 8) and heated at 60°C for 45 minutes for protein reduction. Further, 300 mmol/L iodoacetamide was added to the protein sample and incubated in the dark at room temperature for 45 minutes. The samples were desalted, and to make 500 μL of the sample, 50 μL of 10× New England Biolabs (NEB) glycobuffer 2 buffer was added to prepare a 1× solution. The samples were then treated with 5 μL of PNGase F (NEB), and the mixture was incubated at 37°C for 16 hours to release the N-linked glycans. The N-glycans were recovered by passing the mixture through a C18 cartridge, eluting the N-glycans with 5% acetic acid, and lyophilization. The N-glycans were permethylated by methyl iodide in the presence of sodium hydroxide-dimethyl sulfoxide (NaOH-DMSO) and further analyzed by ESI-MS^n (46).

ESI-MS^n Analysis of Glycans

About 2 μL of permethylated glycans was dissolved in 98 μL of ESI-MS infusion buffer (1:1:1 methanol, 0.1% formic acid in water and acetonitrile) and infused into an Orbitrap Fusion Tribrid mass spectrometer. A precursor scan was acquired at 120,000 resolution, and subsequent collision-induced dissociation (CID) MS^n was acquired for the detailed structural characterization of glycans. For the determination of sialic acid linkages, the glycans were infused with lithium salts for increased cross-ring fragmentation of glycans. The cross-ring fragments of the partially methylated galactose to which the SAs are either 2,3- or 2,6-linked are different and allowed the identification of sialic acid linkages (46).

Glycoproteomics

The glycoproteins were enriched by SNA lectin from membrane fractions as described in the "Western Blotting and Immunoprecipitation" section. Glycoproteins were eluted by boiling in an SDS buffer. The control and knockout samples were run on SDS gel and stained with Coomassie Blue; the gel bands were excised, destained, reduced, and alkylated; and proteins were digested by trypsinization at 37°C for 24 hours. Further, the digested peptides were extracted from the gel pieces, filtered, and evaporated to dryness. The peptides were redissolved in 0.1% formic acid and injected into an Orbitrap Fusion Tribrid mass spectrometer coupled with a Dionex LC system for glycoproteomics analysis. An Acclaim PepMap nano-LC column (Thermo Scientific; 164568) of 150 mm length with 75-μm internal diameter (id), filled with 3 μm, 100Å C18 material (reverse phase), was used for chromatographic separation of peptides. The mass spectrometer method was set up in data-dependent acquisition mode with an MS^1 automatic gain control target value of 5×10^5. After the precursor ion scan at 120,000 resolutions in the Orbitrap analyzer, intense precursors were selected for subsequent fragmentation using higher-energy collision dissociation (HCD) or CID (product-triggered based on the presence of glycan oxonium ions in the HCD) within 3 seconds at a normalized collision energy of 28 and 35, respectively. For internal mass calibration, 445.120025 ion was used as lock mass with a target lock mass abundance of 0%. Charge state screening was enabled, and precursors with an unknown charge state or a charge state of +1 were excluded. Dynamic exclusion was enabled (exclusion size list 100, exclusion duration 30 s). The fragment ions were analyzed in the Orbitrap at 15,000 resolution. The LC-MS/MS chromatogram of control and knockout was analyzed by searching against the human protein database using Byonic 2.3.5 software with variable modifications such as carbamidomethylation of cysteine and oxidation of methionine. Trypsin was chosen as the digestion enzyme, and the human N-glycan database was used for the glycopeptide search. Only glycopeptides with higher scores and good MS/MS fragment ion presence were considered while annotating the proteins. Glycoproteomic data were deposited in glycopost.glycosmos.org with the accession number GPST000273.0 (pin code: 1613).

Cell Clustering Assay

Dissociated PDX primary tumor cells in single-cell suspension were seeded in 96-well plates coated with collagen type I. MDA-MB-231–derived cells were detached with EDTA buffer (0.05 mmol/L), and single cells were seeded in suspension in 96-well plates pretreated with poly-hydroxyethyl methacrylate (Poly-HEMA, Sigma-Aldrich). For the NA treatment, the same number of cells were treated with NA at 0, 10, 50, and 100 mU/mL concentrations. The cells were then incubated and monitored by the IncuCyte live-cell imaging system (Essen BioScience), and images were acquired every 2 hours. Cluster size was analyzed over time by the IncuCyte ZOOM software. In addition, MDA-MB-231 tumor cells were incubated with the anti-PODXL antibody for 30 minutes on ice and imaged using the same experimental method.

Cell Growth Competition Assay

Equal numbers of L2T-ST6WT and L2G-ST6KO or L2G-ST6WT and L2T-ST6KO cells were cultured on the same plate. Cells were counted with flow cytometry on days 0, 6, 18, 25, and 31. Before cell detachment, cells were imaged under a fluorescence microscope. Cells were passaged when they reached 70% to 80% confluence.

Colony Formation Assay

ST6WT and ST6KO cells were cultured in 4-well chambers or 6-well plates (2×10^3 cells) and incubated for a week. Cell cultures were washed gently with PBS and fixed with methanol (25 minutes, 4°C). Next, cells were stained with crystal violet:methanol at the ratio of 1:1 (Sigma-Aldrich and Sigma, respectively). The number and size of the colonies were determined using ImageJ.

Quiescence Assay

ST6WT or ST6KO cells were washed twice with PBS. Cells were stained with pyronin Y (Sigma-Aldrich) according to the manufacturer's protocol. Briefly, 1×10^6 cells were resuspended in 1 mL of PBS containing 2% FBS and 1 μL of pyronin Y solution was added. Cells were then incubated at 37°C for an hour. Then, Hoechst 33342 was added and the cells were incubated for an additional hour. Cells were washed twice with pyronin Y and Hoecsht containing PBS and then stained with lectins or antibodies if necessary or directly loaded onto the flow cytometer.

Cell Viability and Proliferation Assay

To track cell proliferation, a CellTrace CFSE cell proliferation kit (Thermo Fisher) was used. Briefly, equal numbers of ST6WT and ST6KO cells were resuspended in CellTrace CFSE solution (1:1,000 dilution) and incubated for 20 minutes at 37°C in the dark. The complete medium was added to a total volume of 10 mL and further incubated for 5 minutes. Cell suspensions were pelleted and replated on 10-cm plates, and proliferation was analyzed after 24 hours by flow cytometry. For the cell viability assay, because ST6WT and ST6KO cell proliferation rates are different, ST6WT and ST6KO cells were seeded at a ratio of 1:4 in 10-cm plates and grown to a similar confluency on the treatment day. When cells reached 80% confluency, cells were treated with paclitaxel (Sigma) at 0, 10, 25, 50, 100, and 250 μg/mL concentration. Cell viability was measured 24 hours after treatment with DAPI by flow cytometry analysis. To observe time-dependent resistance to paclitaxel, we treated cells with 25 μg/mL paclitaxel and harvested them 0, 8, and 24 hours after treatment. For the treatment of the CTC-PDX-092 model, cells were treated with PAX-NAB at 0, 25, 50, 100, and 250 μg/mL concentrations, and cell death in response to PAX-NAB was measured using DAPI staining by flow cytometry. After SNA sorting (-high and -low), cells were treated with PAX (25 μg/mL) or left untreated and 24 hours after treatment, cellular viability was measured as mentioned above.

Gene Modulation

L2G and L2T dual optical reporter–labeled MDA-MD-231 cells, 4T1 cells, and PDX models were generated as described previously. The CRISPR–Cas9 technique was used to generate ST6KO cells. The gRNA and Cas9–coexpressing lentiviral plasmid targeting human ST6GAL1 gRNA-1 5′ CACCGTCCTACAAGGGGCCGGGACC and gRNA-2 5′ CACCGCATTCACGTGGTCTCGAAGG and control nontarget gRNA were generated by Dr. Derek Abbott (request contact dwa4@case.edu) and kindly gifted by Dr. Brian A. Cobb, Case Western Reserve University. Mouse ST6GAL1-targeting gRNAs, control nontargeting gRNA, and Cas9-expressing plasmids were purchased from Sigma. L2G- or L2T-labeled MDA-MB-231 cells, 4T1 cells, or PDX models were coinfected with appropriate lentiviruses (3 particle-forming units/cell). After 48 hours of infection, cells were selected with puromycin (3 μg/mL). Then cells were sorted for SNA-negative cells. MDA-MB-231 and 4T1 cells were sorted into single cells and plated on 96-well plates to grow single cell–derived clones. For the ST6GAL1-overexpressing cells (ST6OE), full-length ST6GAL1 was inserted into a pEZ-Lv122 vector purchased from GeneCopoeia (EX-M03510Lv122). Virus infection and selection of the cells were performed as described above.

RNA-seq

Total RNA was isolated from ST6WT and ST6KO MDA-MB-231 cells using TRIzol (Thermo Fisher Scientific) according to the

manufacturer's protocol. RNA-seq was performed at the Center for Genetic Medicine Sequencing Core Facility, Northwestern University. RNA-seq was performed on a HiSeq 4000, and a library was made using a TruSeq Total RNA-Seq Library Prep Kit. Data were processed and quantified using STAR (47), DESeq2 (48), and HTSeq (49). Differentially expressed genes were defined by cutoffs of false discovery rate < 0.05 and $\log_2$ (fold change) > 0.48 or < −0.48. Finally, the pathway analysis of significantly differentially expressed genes was obtained using Metascape (http://metascape.org; ref. 50). The data are accessible at the Gene Expression Omnibus (GEO) with accession number GSE174080 (release date: Dec 1, 2022).

Cell-Binding Assay

MDA-MB-231 cells (ST6WT and ST6KO) were plated in 96 wells/plate (2×10^4 cells/well) and cultured overnight, and the next day after cells were attached completely, cells were washed with PBS twice. On the other hand, membranes of the ST6WT and ST6KO cells were fractionated according to the protocol indicated above. Endogenous PODXL was pulled down using an anti-PODXL antibody (Santa Cruz Biotechnology, 3D3, sc-23904). Glycine (0.1 mol/L, pH 2.5) was utilized for antibody/antigen (anti-PODXL/PODXL) release from agarose beads. Acidic condition was neutralized immediately by adding Tris-HCl (1 mol/L, pH 8.8). Purified complexes were then labeled with HRP (EZ-Link plus activated peroxidase kit, Thermo Fisher, 31489) according to the provided protocol. HRP-labeled purified PODXL from ST6WT and ST6KO cells was added onto the cells and incubated for 1 to 2 hours at 37°C. Cell–protein complexes were then washed with PBS 5 times. TMB substrate solution (Thermo Scientific, N301) and stop solution (Thermo Scientific, N600) were used to visualize the protein binding to the cells (absorbance were measured at 450 nm).

Transendothelial Cell Migration

Transendothelial cell migration of cancer cells through HUVECs was quantified as described previously (35, 51). Briefly, HUVECs were grown on hydrated collagen gels until confluent. ST6WT and ST6KO MDA-MB-231 cells were added to the medium. The cells were allowed to transmigrate for 3 hours at 37°C. Then, the suspending cells were washed with PBS and plates were fixed with 10% neutral buffered formalin. Cells on the top of the HUVEC and the cells that migrated through HUVECs were counted.

Quantification of Total Intensity of CellSearch Images

The images of the individual cells collected by CellSearch analysis were analyzed using ImageJ software manually. The mean intensity was multiplied by the total area to find the total intensity of DAPI. The cutoff value of the binary assessment of Ki-67–negative cells was <75. Cell-cycle determination using DAPI intensity was as follows: G_1/G_0 ≤100.000, G_2–M 100.001–139.999, and S phase ≥140.000. The correlation of DAPI versus Ki-67/SNA was calculated using www.socscistatistics.com.

Statistical Analysis

Categorical variables were reported as frequency distributions, whereas continuous variables were described through median and interquartile ranges. Matched pair variations of cluster enumerations were tested across baseline and E1 through the Wilcoxon signed rank test. Patient data analysis was conducted using StataCorp 2019 Stata Statistical Software (Release 16.1), R (version 4.1.0, The R foundation for Statistical Computing), and JMP (version 16, SAS Institute). Microsoft Excel and GraphPad Prism were used to perform Student *t* test and calculate *P* values for all *in vitro* assays and analyses unless specified otherwise. $P \le 0.05$ was considered statistically significant and is represented with * for $P \le 0.05$, ** for $P \le 0.01$, *** for $P \le 0.001$, and **** for $P \le 0.0001$. Data are presented as mean ± standard deviation (SD) unless specified otherwise.

Data Availability

All of the data included in this article are available upon request. The data generated in this study are publicly available in glycopost.glycosmos.org at GPST000273.0 (pin code: 1613) and in the GEO at GSE174080. RRID numbers and more detailed information on commercially available antibodies and reagents are included in Supplementary Excel S6.

Authors' Disclosures

L. Gerratana reports personal fees from Eli Lilly, Novartis, Pfizer, GSK, Daiichi Sankyo, AstraZeneca, and Incyte outside the submitted work. V. Adorno-Cruz reports personal fees from Biotheranostics, a Hologic company, outside the submitted work. C. Reduzzi reports grants from Menarini Silicon Biosystems outside the submitted work. L. El-Shennaway reports grants from the NIH during the conduct of the study, as well as a patent for the area of exosome therapeutics pending. P. D'Amico reports grants from Roche and other support from Merck & Co. outside the submitted work. A.N. Shah reports personal fees from Gilead and AstraZeneca outside the submitted work. M. Cristofanilli reports personal fees from Menarini and grants from Predicine during the conduct of the study, as well as personal fees from Pfizer, AstraZeneca, and Datar Genetics outside the submitted work. W.A. Muller reports grants from the NIH during the conduct of the study. B.A. Cobb reports grants from the NIH during the conduct of the study, as well as grants from the NIH outside the submitted work. H. Liu reports nonfinancial support and other support from ExoMira Medicine outside the submitted work, as well as a patent for anti-PODXL to block CTC cluster formation and metastatic seeding pending. No disclosures were reported by the other authors.

Authors' Contributions

N.K. Dashzeveg: Conceptualization, resources, data curation, software, formal analysis, validation, investigation, visualization, methodology, writing–original draft, project administration, writing–review and editing. **Y. Jia:** Supervision, validation, investigation. **Y. Zhang:** Resources, validation. **L. Gerratana:** Resources, data curation, formal analysis, validation, visualization. **P. Patel:** Resources, validation, visualization. **A. Shajahan:** Resources, validation, investigation, visualization. **T. Dandar:** Formal analysis, validation, investigation, visualization. **E.K. Ramos:** Formal analysis, validation, visualization, writing–original draft. **H.F. Almubarak:** Resources, data curation, formal analysis, methodology. **V. Adorno-Cruz:** Formal analysis, visualization, methodology, writing–original draft. **R. Taftaf:** Formal analysis, methodology. **E.J. Schuster:** Formal analysis, methodology. **D. Scholten:** Resources, formal analysis. **M.T. Sokolowski:** Data curation, formal analysis, validation. **C. Reduzzi:** Resources, formal analysis. **L. El-Shennawy:** Resources, data curation, formal analysis, methodology. **A.D. Hoffmann:** Data curation, formal analysis, investigation, methodology. **M. Manai:** Resources, formal analysis, validation. **Q. Zhang:** Resources, formal analysis, supervision. **P. D'Amico:** Formal analysis, supervision. **P. Azadi:** Resources, supervision, validation. **K.J. Colley:** Resources, supervision. **L.C. Platanias:** Resources, supervision, validation. **A.N. Shah:** Resources, supervision. **W.J. Gradishar:** Resources, supervision, investigation, writing–review and editing. **M. Cristofanilli:** Conceptualization, resources, data curation, software, formal analysis, supervision, validation, visualization, methodology, writing–original draft, project administration, writing–review and editing. **W.A. Muller:** Resources, data curation, investigation, methodology, writing–review and editing. **B.A. Cobb:** Resources, data curation, supervision, methodology. **H. Liu:** Conceptualization, resources, data curation,

software, formal analysis, supervision, validation, investigation, visualization, methodology, writing–original draft, project administration, writing–review and editing.

Acknowledgments

We are grateful to Dr. Susan L. Bellis at the University of Alabama at Birmingham for her insightful feedback and suggestions for this project. We thank Dr. Derek W. Abbott at Case Western Reserve University for generating and providing gRNAs for CRISPR–Cas9-mediated KO of ST6GAL1 (R21 DE025825 to D.W. Abbott and B.A. Cobb). We acknowledge the tremendous support from the Northwestern Core facilities of CTC Core, the Center for Comparative Medicine, Small Animal Imaging, Microscopy Imaging, Lurie Cancer Center Flow Core, NUSeq Core and Bioinformatics Center, Mouse Histology and Phenotyping Laboratory, and the Pathology Core, as well as the Glycomic Mass Spectrometry Facilities at the Complex Carbohydrate Research Center, the University of Georgia. This work was partially funded by the Department of Defense (BC150596 and BC190982; H. Liu), the NIH (R01CA245699 to H. Liu; R01 GM115234 to B.A. Cobb; and S10OD018530 and R24GM137782 to P. Azadi), the American Cancer Society (ACS127951-RSG-15-025-01-CSM), the Komen Foundation (CCR15332826), the H Foundation, the Lynn Sage Breast Cancer Foundation (H. Liu and N. Dashzeveg), and a Northwestern University start-up grant (H. Liu).

The publication costs of this article were defrayed in part by the payment of publication fees. Therefore, and solely to indicate this fact, this article is hereby marked "advertisement" in accordance with 18 USC section 1734.

Note

Supplementary data for this article are available at Cancer Discovery Online (http://cancerdiscovery.aacrjournals.org/).

Received June 3, 2022; revised April 14, 2023; accepted May 30, 2023; published first June 5, 2023.

REFERENCES

1. Cheung KJ, Padmanaban V, Silvestri V, Schipper K, Cohen JD, Fairchild AN, et al. Polyclonal breast cancer metastases arise from collective dissemination of keratin 14-expressing tumor cell clusters. Proc Natl Acad Sci U S A 2016;113:E854–63.
2. Mu Z, Wang C, Ye Z, Austin L, Civan J, Hyslop T, et al. Prospective assessment of the prognostic value of circulating tumor cells and their clusters in patients with advanced-stage breast cancer. Breast Cancer Res Treat 2015;154:563–71.
3. Aceto N, Bardia A, Miyamoto DT, Donaldson MC, Wittner BS, Spencer JA, et al. Circulating tumor cell clusters are oligoclonal precursors of breast cancer metastasis. Cell 2014;158:1110–22.
4. Liu X, Taftaf R, Kawaguchi M, Chang YF, Chen W, Entenberg D, et al. Homophilic CD44 interactions mediate tumor cell aggregation and polyclonal metastasis in patient-derived breast cancer models. Cancer Discov 2019;9:96–113.
5. Zoller M. CD44: can a cancer-initiating cell profit from an abundantly expressed molecule? Nat Rev Cancer 2011;11:254–67.
6. Vagia E, Mahalingam D, Cristofanilli M. The landscape of targeted therapies in TNBC. Cancers (Basel) 2020;12:916.
7. Foulkes WD, Smith IE, Reis-Filho JS. Triple-negative breast cancer. N Engl J Med 2010;363:1938–48.
8. Liu H, Patel MR, Prescher JA, Patsialou A, Qian D, Lin J, et al. Cancer stem cells from human breast tumors are involved in spontaneous metastases in orthotopic mouse models. Proc Natl Acad Sci U S A 2010;107:18115–20.
9. Gianni L, Baselga J, Eiermann W, Guillem Porta V, Semiglazov V, Lluch A, et al. Feasibility and tolerability of sequential doxorubicin/paclitaxel followed by cyclophosphamide, methotrexate, and fluorouracil and its effects on tumor response as preoperative therapy. Clin Cancer Res 2005;11:8715–21.
10. Kalinsky K, Barlow WE, Gralow JR, Meric-Bernstam F, Albain KS, Hayes DF, et al. 21-Gene assay to inform chemotherapy benefit in node-positive breast cancer. N Engl J Med 2021;385:2336–47.
11. Gianni L, Baselga J, Eiermann W, Porta VG, Semiglazov V, Lluch A, et al. Phase III trial evaluating the addition of paclitaxel to doxorubicin followed by cyclophosphamide, methotrexate, and fluorouracil, as adjuvant or primary systemic therapy: European Cooperative Trial in Operable Breast Cancer. J Clin Oncol 2009;27:2474–81.
12. Rastogi P, Anderson SJ, Bear HD, Geyer CE, Kahlenberg MS, Robidoux A, et al. Preoperative chemotherapy: updates of National Surgical Adjuvant Breast and Bowel Project Protocols B-18 and B-27. J Clin Oncol 2008;26:778–85.
13. Miles D, Gligorov J, Andre F, Cameron D, Schneeweiss A, Barrios C, et al. Primary results from IMpassion131, a double-blind, placebo-controlled, randomised phase III trial of first-line paclitaxel with or without atezolizumab for unresectable locally advanced/metastatic triple-negative breast cancer. Ann Oncol 2021;32:994–1004.
14. Cortes J, Cescon DW, Rugo HS, Nowecki Z, Im SA, Yusof MM, et al. Pembrolizumab plus chemotherapy versus placebo plus chemotherapy for previously untreated locally recurrent inoperable or metastatic triple-negative breast cancer (KEYNOTE-355): a randomised, placebo-controlled, double-blind, phase 3 clinical trial. Lancet 2020;396:1817–28.
15. Taftaf R, Liu X, Singh S, Jia Y, Dashzeveg NK, Hoffmann AD, et al. ICAM1 initiates CTC cluster formation and trans-endothelial migration in lung metastasis of breast cancer. Nat Commun 2021;12:4867.
16. Schuster E, Taftaf R, Reduzzi C, Albert MK, Romero-Calvo I, Liu H. Better together: circulating tumor cell clustering in metastatic cancer. Trends Cancer 2021;7:1020–32.
17. Ramos EK, Tsai CF, Jia Y, Cao Y, Manu M, Taftaf R, et al. Machine learning-assisted elucidation of CD81-CD44 interactions in promoting cancer stemness and extracellular vesicle integrity. Elife 2022;11:e82669.
18. Pinho SS, Reis CA. Glycosylation in cancer: mechanisms and clinical implications. Nat Rev Cancer 2015;15:540–55.
19. Reily C, Stewart TJ, Renfrow MB, Novak J. Glycosylation in health and disease. Nat Rev Nephrol 2019;15:346–66.
20. Li F, Ding J. Sialylation is involved in cell fate decision during development, reprogramming and cancer progression. Protein Cell 2019;10:550–65.
21. Garnham R, Scott E, Livermore KE, Munkley J. ST6GAL1: a key player in cancer. Oncol Lett 2019;18:983–9.
22. Jones RB, Dorsett KA, Hjelmeland AB, Bellis SL. The ST6Gal-I sialyltransferase protects tumor cells against hypoxia by enhancing HIF-1alpha signaling. J Biol Chem 2018;293:5659–67.
23. Swindall AF, Bellis SL. Sialylation of the Fas death receptor by ST6Gal-I provides protection against Fas-mediated apoptosis in colon carcinoma cells. J Biol Chem 2011;286:22982–90.
24. Britain CM, Holdbrooks AT, Anderson JC, Willey CD, Bellis SL. Sialylation of EGFR by the ST6Gal-I sialyltransferase promotes EGFR activation and resistance to gefitinib-mediated cell death. J Ovarian Res 2018;11:12.
25. Smerage JB, Barlow WE, Hortobagyi GN, Winer EP, Leyland-Jones B, Srkalovic G, et al. Circulating tumor cells and response to chemotherapy in metastatic breast cancer: SWOG S0500. J Clin Oncol 2014;323483–9.
26. Tsai CF, Zhang P, Scholten D, Martin K, Wang YT, Zhao R, et al. Surfactant-assisted one-pot sample preparation for label-free single-cell proteomics. Commun Biol 2021;4:265.
27. Dorsett KA, Jones RB, Ankenbauer KE, Hjelmeland AB, Bellis SL. Sox2 promotes expression of the ST6Gal-I glycosyltransferase in ovarian cancer cells. J Ovarian Res 2019;12:93.
28. Schultz MJ, Holdbrooks AT, Chakraborty A, Grizzle WE, Landen CN, Buchsbaum DJ, et al. The tumor-associated glycosyltransferase ST6Gal-I regulates stem cell transcription factors and confers a cancer stem cell phenotype. Cancer Res 2016;76:3978–88.
29. Swindall AF, Londono-Joshi AI, Schultz MJ, Fineberg N, Buchsbaum DJ, Bellis SL. ST6Gal-I protein expression is upregulated in human epithelial

tumors and correlates with stem cell markers in normal tissues and colon cancer cell lines. Cancer Res 2013;73:2368–78.
30. Johnson DG, Schwarz JK, Cress WD, Nevins JR. Expression of transcription factor E2F1 induces quiescent cells to enter S phase. Nature 1993;365:349–52.
31. Kwon JS, Everetts NJ, Wang X, Wang W, Della Croce K, Xing J, et al. Controlling depth of cellular quiescence by an Rb-E2F network switch. Cell Rep 2017;20:3223–35.
32. Poppy Roworth A, Ghari F, La Thangue NB. To live or let die - complexity within the E2F1 pathway. Mol Cell Oncol 2015;2:e970480.
33. Nagy A, Lanczky A, Menyhart O, Gyorffy B. Validation of miRNA prognostic power in hepatocellular carcinoma using expression data of independent datasets. Sci Rep 2018;8:9227.
34. Weber EW, Han F, Tauseef M, Birnbaumer L, Mehta D, Muller WA. TRPC6 is the endothelial calcium channel that regulates leukocyte transendothelial migration during the inflammatory response. J Exp Med 2015;212:1883–99.
35. Muller WA, Weigl SA, Deng X, Phillips DM. PECAM-1 is required for transendothelial migration of leukocytes. J Exp Med 1993;178:449–60.
36. Liu X, Adorno-Cruz V, Chang YF, Jia Y, Kawaguchi M, Dashzeveg NK, et al. EGFR inhibition blocks cancer stem cell clustering and lung metastasis of triple negative breast cancer. Theranostics 2021;11:6632–43.
37. Cherian S, Potdar V, Jadhav S, Yadav P, Gupta N, Das M, et al. SARS-CoV-2 spike mutations, L452R, T478K, E484Q and P681R, in the second wave of COVID-19 in Maharashtra, India. Microorganisms 2021;9:1542.
38. Karagiannis GS, Pastoriza JM, Wang Y, Harney AS, Entenberg D, Pignatelli J, et al. Neoadjuvant chemotherapy induces breast cancer metastasis through a TMEM-mediated mechanism. Sci Transl Med 2017;9:eaan0026.
39. Dong QG, Sclabas GM, Fujioka S, Schmidt C, Peng B, Wu T, et al. The function of multiple IkappaB: NF-kappaB complexes in the resistance of cancer cells to Taxol-induced apoptosis. Oncogene 2002;21:6510–9.
40. Wei A, Fan B, Zhao Y, Zhang H, Wang L, Yu X, et al. ST6Gal-I overexpression facilitates prostate cancer progression via the PI3K/Akt/GSK-3beta/beta-catenin signaling pathway. Oncotarget 2016;7:65374–88.
41. Christie DR, Shaikh FM, Lucas JA 4th, Lucas JA 3rd, Bellis SL. ST6Gal-I expression in ovarian cancer cells promotes an invasive phenotype by altering integrin glycosylation and function. J Ovarian Res 2008;1:3.
42. Jung YR, Park JJ, Jin YB, Cao YJ, Park MJ, Kim EJ, et al. Silencing of ST6Gal I enhances colorectal cancer metastasis by down-regulating KAI1 via exosome-mediated exportation and thereby rescues integrin signaling. Carcinogenesis 2016;37:1089–97.
43. Zhang S, Lu J, Xu Z, Zou X, Sun X, Xu Y, et al. Differential expression of ST6GAL1 in the tumor progression of colorectal cancer. Biochem Biophys Res Commun 2017;486:1090–6.
44. Cristofanilli M, Budd GT, Ellis MJ, Stopeck A, Matera J, Miller MC, et al. Circulating tumor cells, disease progression, and survival in metastatic breast cancer. N Engl J Med 2004;351:781–91.
45. Allard WJ, Matera J, Miller MC, Repollet M, Connelly MC, Rao C, et al. Tumor cells circulate in the peripheral blood of all major carcinomas but not in healthy subjects or patients with nonmalignant diseases. Clin Cancer Res 2004;10:6897–904.
46. Shajahan A, Supekar NT, Chapla D, Heiss C, Moremen KW, Azadi P. Simplifying glycan profiling through a high-throughput micropermethylation strategy. SLAS Technol 2020;25:367–79.
47. Dobin A, Davis CA, Schlesinger F, Drenkow J, Zaleski C, Jha S, et al. STAR: ultrafast universal RNA-seq aligner. Bioinformatics 2013;29:15–21.
48. Love MI, Huber W, Anders S. Moderated estimation of fold change and dispersion for RNA-seq data with DESeq2. Genome Biol 2014;15:550.
49. Anders S, Pyl PT, Huber W. HTSeq–a Python framework to work with high-throughput sequencing data. Bioinformatics 2015;31:166–9.
50. Tripathi S, Pohl MO, Zhou Y, Rodriguez-Frandsen A, Wang G, Stein DA, et al. Meta- and orthogonal integration of influenza "OMICs" data defines a role for UBR4 in virus budding. Cell Host Microbe 2015;18:723–35.
51. Muller WA, Luscinskas FW. Assays of transendothelial migration in vitro. Methods Enzymol 2008;443:155–76.